Advancing Breast Cancer Detection: Embedding Nanoparticles into Breast Phantoms for Diagnostic Applications

MS Thesis

By

MISBAH ASHIQ

CUI/SP24-RPH-012/LHR

COMSATS University Islamabad

Lahore Campus–Pakistan

Spring 2025

Advancing Breast Cancer Detection: Embedding Nanoparticles into Breast Phantoms for Diagnostic Applications

A Thesis submitted to

COMSATS University Islamabad

In partial fulfillment of the requirement for the degree of

Master of Science in

Physics

By

MISBAH ASHIQ

CUI/SP24-RPH-012/LHR

Fall 2026

Advancing Breast Cancer Detection: Embedding Nanoparticles into Breast Phantoms for Diagnostic Applications

This Thesis submitted to the Department of Physics as partial fulfillment of the requirement for the award of Degree of Master of Science in Physics

Name	Registration Number
MISBAH ASHIQ	CUI/SP24-RPH-012/LHR

Supervisory Committee

Supervisor

Dr. Naima Amin

Associate Professor

Department of Physics

CUI, Lahore Campus

Co-Supervisor

Dr. Ghazanfar Abbas

Associate Professor

Department of Physics

CUI, Lahore Campus

Certificate of Approval

This thesis is titled

Advancing Breast Cancer Detection: Embedding Nanoparticles into Breast Phantoms for Diagnostic Applications

By

MISBAH ASHIQ

CUI/SP24-RPH-012/LHR

has been approved for the degree of MS Physics at COMSATS University Islamabad, Lahore Campus

External Examiner: _____

Supervisor: _____

Dr. Naima Amin

Associate Professor, Department of Physics, CUI, Lahore Campus

Co-Supervisor: _____

Dr. Ghazanfar Abbas

Associate Professor, Department of Physics, Lahore Campus

Head of Department: _____

Dr. Aamir Razaq

HOD (Department of Physics) CUI, Lahore Campus

Author's Declaration

I **Misbah Ashiq**, (**CUI/SP24-RPH-012/LHR**), hereby declare that I have produced the work presented in this thesis, during the scheduled period of study. I also declare that I have not taken any material from any source except referred to wherever due to that amount of plagiarism is within an acceptable range. If a violation of HEC rules on research has occurred in this thesis, I shall be liable to punishable action under the plagiarism rules of HEC.

Date: _____

Signature of the student

_____

Misbah Ashiq

CUI/SP24-RPH-012/LHR

Certificate

It is certified that **Misbah Ashiq** Registration Number (**CUI/SP24-RPH-012/LHR**) has carried out all the research work related to this thesis under my supervision at the Department of Physics, COMSATS University Islamabad, Lahore Campus and the work fulfill the requirement for the award of the MS in Physics.

Date: _____

Supervisor:

_____

Dr. Naima Amin

Associate Professor

Department of Physics
COMSATS University Islamabad, Lahore Campus

IN THE NAME OF ALLAH,

THE MOST BENEFICENT,

THE MOST MERCIFUL.

DEDICATIONS

First and foremost, I am deeply grateful to **Almighty Allah** for granting me the strength, patience, and guidance to complete this work. I wholeheartedly dedicate this thesis to the **blessed memory of my beloved parents**, whose sacrifices, prayers, and values continue to guide and inspire me every day. May Allah grant them the highest place in Jannah. Ameen.

With my deepest gratitude and warmest affection, I also dedicate this work to **Dr. Naima Amin** and **Dr. Ghazanfar Abbas**. Without their courageous inspiration, continuous support, and intellectual guidance, this research would not have been possible.

I further extend this dedication to my **respected teachers**, whose direction and mentorship have been a constant source of knowledge and motivation, and to my **supportive friends**, who stood by me throughout this journey.

ACKNOWLEDGEMENTS

"One who follows a path to seek knowledge has his path to Paradise made easy by ALLAH" (Hadith)

All admire and thanks to ALLAH, the lord of humankind and all that exists, for all his blessings, decency, guidance at every stage of our life. Who blessed us courage, strength, and audacity to complete this work in less time.

It is an honor for me to express deep gratitude and respect to **Prof Dr. Amir Razaq** of Physics Department at CUI, Lahore Campus, for providing us all kinds of project facilities and for his valuable support.

I would like to express my sincere gratitude to my supervisors, **Dr. Naima Amin** and **Dr. Ghazanfar Abbas**, for their continuous support, expert supervision, and valuable insights throughout the course of this study. Their encouragement, patience, and constructive feedback were vital in shaping this research.

I also gratefully acknowledge all the **faculty members** and **technical staff** at **COMSATS University Islamabad, Lahore Campus**, for providing the resources, facilities, and an environment conducive to academic excellence.

My heartfelt thanks go to the **blessed memory of my late parents**, whose prayers, sacrifices, and love remain the foundation of my success. May Allah (SWT) grant them the highest place in Jannah. Ameen.

Finally, I would like to extend my appreciation to my **friends and colleagues** for their unwavering support, motivation, and companionship throughout this journey.

Misbah Ashiq (CUI/SP24-RPH-012/LHR)

ABSTRACT

Advancing Breast Cancer Detection: Embedding Nanoparticles into Breast Phantoms for Diagnostic Applications

By

Misbah Ashiq

In this study, a single-layer homogeneous breast tumor phantom was developed to simulate the diagnostic properties of malignant breast tissue, with the aim of enhancing breast cancer detection and diagnostic accuracy. The tumor-mimicking phantom was fabricated using an optimized gelatin-based hydrogel, incorporating additives such as NaCl, PVA, glycerin, agar, ethanol, and PEG to reproduce the physical consistency and imaging characteristics of tumor tissue. Silver oxide (Ag_2O) and iron oxide (Fe_3O_4) nanoparticles were synthesized using controlled chemical methods and characterized using FTIR, XRD, and SEM to confirm their chemical composition, crystalline structure, and surface morphology, ensuring their suitability for diagnostic imaging applications. The nanoparticles were uniformly incorporated into the tumor phantom through a premixing approach, resulting in a homogeneous distribution that simulates nanoparticle-enhanced tumor tissue. The fabricated tumor phantoms were evaluated using computed tomography (CT) to assess their effectiveness in breast cancer detection. CT imaging demonstrated increased Hounsfield Unit values due to the high atomic number of silvers in Ag_2O nanoparticles, leading to enhanced X-ray attenuation, while MRI scans revealed clear signal suppression and contrast variation in Fe_3O_4-loaded phantoms owing to their superparamagnetic properties. The results confirm that the developed single-layer homogeneous tumor phantom provides a reliable and reproducible model for evaluating nanoparticle-assisted breast cancer detection and precise diagnosis, offering a simplified yet effective platform for imaging system calibration, contrast agent assessment, and preclinical diagnostic studies.

Key Words: Breast tumor phantom, Radiotherapy, Tissue-mimicking materials, Nanoparticle embedding, CT imaging.

Contents

Chapter 1 Introduction

In recent years, research indicates that cancer now exceeds other fatal conditions to become the dominant cause of mortality globally[1]. Breast cancer represents the most prevalent and lethal form of cancer seen in women while it causes numerous cancer deaths each year[2], [3].

Despite remarkable development in medical technology, the difficulties related to early detection and precise diagnosis of breast cancer are still unfixed. Therefore, to improve clinical results, it is necessary to develop novel diagnostic approaches[3]. A major concern during breast cancer diagnosis is the risk of missing early-stage tumors or misidentifying benign tissues as malignant, which may delay timely treatment. Precise diagnostic outcomes are made more difficult by the biological complexity and variety of tumor cells[4].

Despite significant cutting-edge medical research, there are still difficulties with early detection and precise diagnosis of breast cancers. Early detection is essential since accurate diagnosis improves treatment outcomes and significantly increases the chance of survival. Thus, novel diagnostic methods that can precisely identify tumor regions in their early stage prior to their development are necessary[5].

To address this issue, we are focusing on the development of tissue-equivalent phantoms that can simulate human body tissues. These phantoms serve as essential instruments to evaluate diagnostic imaging systems, enabling researchers improve accuracy, sensitivity, and tumor localization before their clinical application[6].

Nanoparticles are currently gaining a lot of attention in biomedical research because of their unique physical and chemical properties features, biocompatibility, and contrast-enhancing characteristics. Researchers are currently examining metal oxide nanoparticles as contrast agents to increase the diagnostic accuracy of breast cancers in imaging modalities such as CT, MRI, and ultrasound[7].

This study investigates the fabrication of a breast tumor-mimicking phantom enhanced with silver oxide (Ag_2O) and iron oxide (Fe_3O_4) nanoparticles to improve diagnostic imaging contrast and properly mimic tumor tissue characteristics. Our aim is to design

and develop a breast tumor phantom embedded with nanoparticles to enhance early detection and localization while minimizing damage to healthy tissues[8], [9].

1.1 Main Objective

Breast cancer remains one of the most prevalent and life-threatening diseases among women worldwide, and early detection is essential for improving treatment outcomes. Despite advancements in imaging technologies, challenges such as low contrast, unclear tumor boundaries, and limited tissue representation still restrict accurate diagnosis. This research addresses these limitations by developing a specialized breast tumor phantom embedded with nanoparticles to enhance diagnostic precision.

In this study, a homogeneous tumor tissue layer was fabricated to replicate the physical and radiological properties of real tumor tissue. To enhance its imaging visibility, two types of synthesized nanoparticles iron oxide and silver oxide were embedded within the tumor layer. These nanoparticles were selected due to their favorable atomic characteristics, which significantly improve imaging contrast and allow clearer differentiation between healthy and malignant regions during diagnostic scans.

After fabrication, the tumor phantom underwent imaging evaluations to determine how nanoparticle incorporation influenced contrast enhancement and signal response. As a controlled, repeatable model, the phantom simulates clinical behavior without exposing real patients to radiation, making it a valuable tool for studying imaging performance and diagnostic improvements.

In summary, the primary objective of this research is to develop a nanoparticle-enhanced breast tumor phantom designed for diagnostic applications. By integrating iron oxide and silver oxide nanoparticles into a homogeneous tumor tissue layer, the study aims to improve imaging sensitivity, contrast resolution, and overall accuracy in breast cancer detection.

1.2 Tumor:

The result of cancer arises from mutations which make cells uncontrollably grow into tumors. Human beings experience a normal cell cycle which includes cell division

along with growth while simultaneously replicating themselves to replace degenerated cell components. Cells receive three types of signals in the human body: death signals after damage and growth signals along with expansion signals. However, cancer cells behave differently from normal ones. The body does not need these abnormal cells, yet they survive and continue to reproduce and multiply. More abnormal cells emerge from this to form a tumor. A tumor, also called neoplasm, is a mass of tissues formed because of excessive growth of abnormal Cells. It is an abnormal growth of cells that have no functional purposes and has the potential to spread to different organs or other parts of the body[10].

1.2.1 Types of Tumors:

There are various classifications for tumors based on their tissue of origin and cell types. Tumors are typically categorized into two main types: benign tumors and malignant tumors.

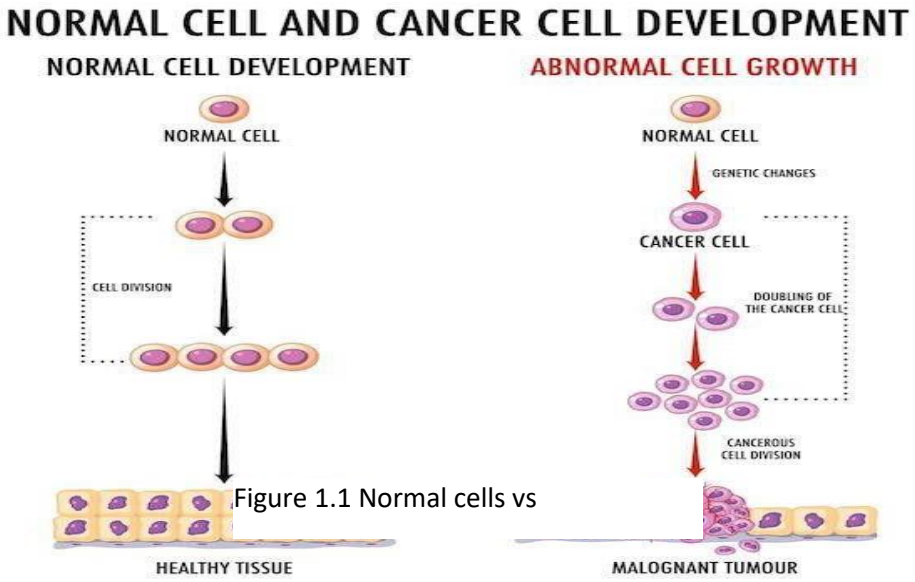

Figure 1.1 Normal cells vs

Figure 1.1 Normal Cells Vs Cancer Cells

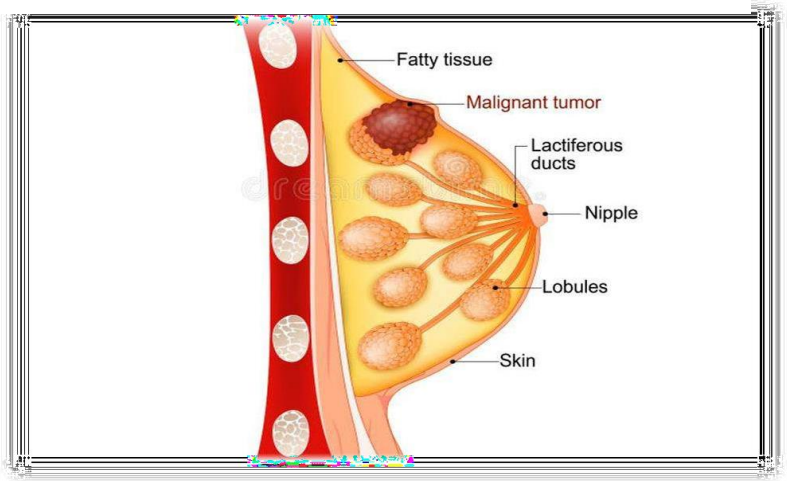

1.2.2 Benign Tumor:

The nature of benign tumors is their complete localization within a single area without spreading to different anatomical regions. Benign tumors remain in their original location while avoiding both regional growth as well as spreading to different body regions. The growth of benign tumors occurs slowly while forming distinct boundary areas. The characteristics of benign tumors do not typically cause difficulties for the body. The increase in size of benign tumors can lead to nearby structure compression which often produces pain and other medical issues.

A significant benign lung tumor can cause respiratory distress because it forms compressive pressure on the trachea (windpipe) thus leading to breathing difficulties. The patient requires urgent surgical treatment at this point. Removal of benign tumors eliminates their possibility to reappear. Benign tumors possess the ability to develop into malignant conditions. Continuous observation determines if surgical removal becomes necessary[10].

1.2.3 Malignant Tumor:

A malignant tumor can invade and overcome surrounding normal tissues and spread throughout the body, also called metastasis. Resulting tumors are classified as harmful and cancerous tumors. The growth pattern of this tumor cannot be controlled because it travels throughout the bloodstream. The movement of malignant tumors between different areas of the body causes treatment resistance at those locations. Treatment through surgery combined with chemotherapy and radiation therapy serves as the main approach to address these tumors when doctors detect them at early body locations.

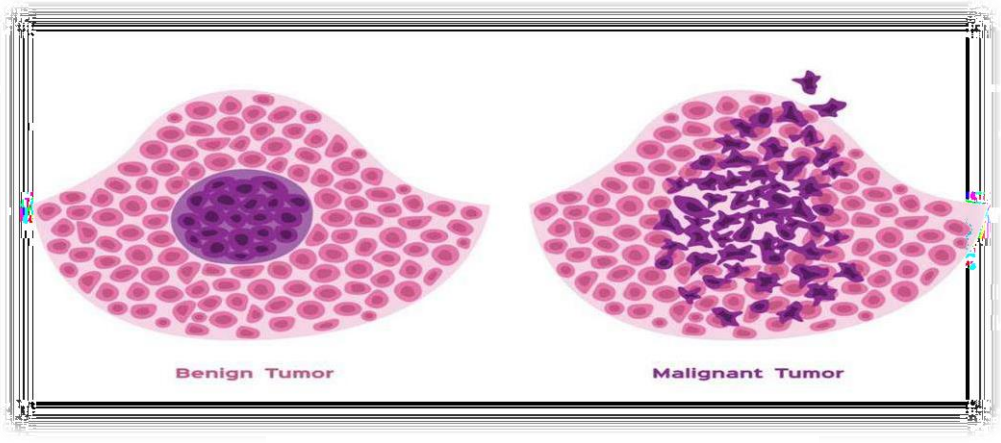

Figure 1.2 Benign tumor vs malignant tumor

1.3 Anatomy of breast:

The human breast exists as a specialized organ that consists mostly of glandular tissue together with fibrous tissue and adipose tissue for milk production and delivery functions. The glandular section contains lobes together with lobules. Every breast carries 15–20 lobes which organize themselves near the nipple. Milk moves from the lobules to the nipples through a duct chain which combines into lactiferous ducts.

Fibrous tissue supports the shape of the breast. To support breast structure and maintain breast shape fibrous tissue develop ligaments that work as bands of connective tissue. The breast ligaments stretch with time which results in

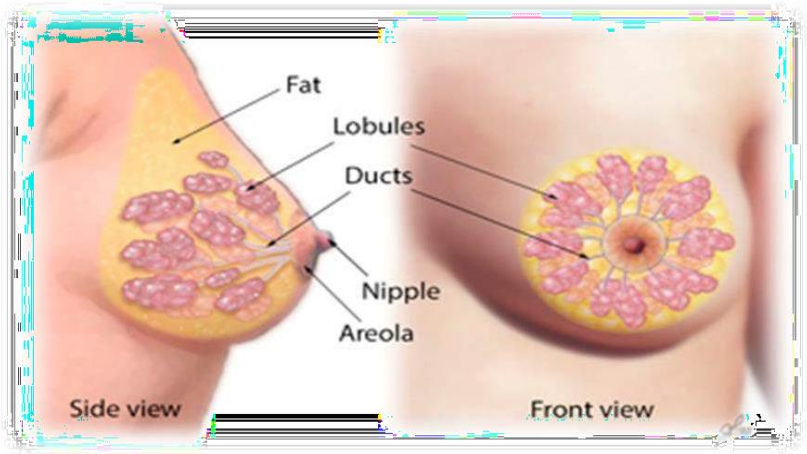

Figure 1.3 Anatomy of breast

modifications to breast shape. Adipose (Fatty) tissue located near the lobules and

ducts, covering the area between glandular tissues. The size and shape of the breast is determined by the number of adipose tissues but does not have ability to affect the production of milk[11].

1.4 Breast Cancer

Breast tumor is a cancer that arises in the breast tissues milk ducts and lobules. They usually occur by the cells mutate and grow uncontrollably, creating a mass called tumor. It can be either benign or malignant breast tumors. One out of ten of all diagnosed cancers worldwide is the cancer of the female breast. It is considered the

second most common cause of death due to cancer in the women.

Breast cancers typically originate in the cells of lobules, and they can occur in various areas of the breast. In some cases, they have the potential to spread to other parts of the body, forming what is known as a secondary tumor. These secondary tumors are classified as malignant. On the other hand, benign breast tumors are non-cancerous, meaning they do not have the capacity to spread to other body parts; they remain localized. However, they can bring about changes in the breast and may exhibit symptoms such as breast pain, thickening, and swelling. One common type of benign breast tumor is fibro adenoma, which often necessitates surgical removal for treatment.

Malignant tumors, in contrast, are cancerous and could metastasize other parts of the body. If not promptly treated, they can be highly detrimental, spreading through muscles and bones. Malignant tumors can also occur on the skin of the breast[12].

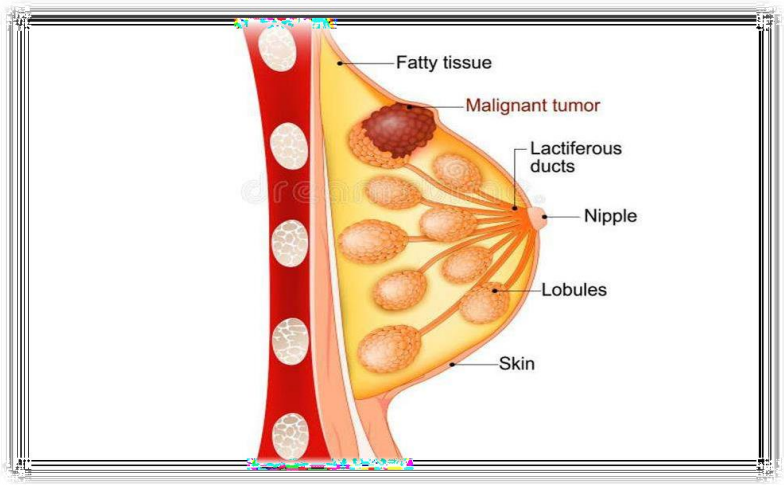

Figure 1.4 Breast Cancer

1.5 Kinds of Breast cancer:

There are mainly two types of breast cancers with their subtypes. It can be further classified as either invasive or non-invasive Different factors affect the type of

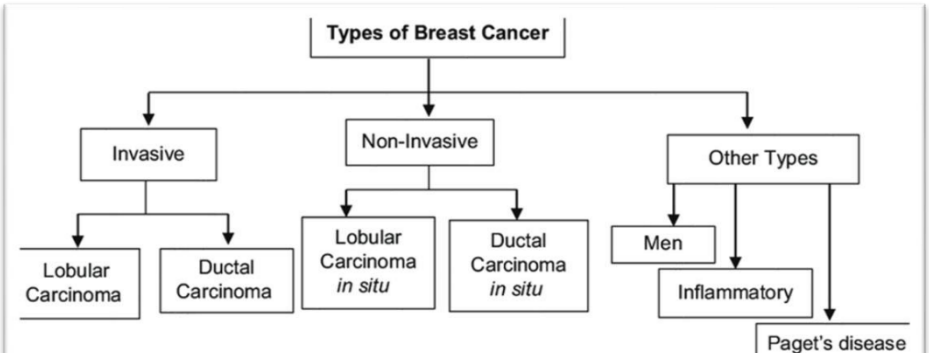

Figure 1.5 Types Of Breast Cancer

tumor, including age, size, stage, grade, etc.

1.6 Invasive Breast cancer:

Most breast cancers are invasive in which cancer spreads to other sites of the breast tissues like lymph nodes. These cancer cells in the ducts and lobular walls invade the surrounding tissues like fatty and connective tissues of the breast. Invasive breast cancer refers to cancer that has spread beyond its original location, typically from the milk ducts (in ductal carcinoma) or lobules (in lobular carcinoma) to the surrounding breast tissue. These cancer cells can then enter the lymphatic system or bloodstream, potentially leading to metastasis in other parts of the body. The spread often involves the lymph nodes, which are crucial in diagnosing the stage of cancer and determining treatment options. Early detection of invasive breast cancer is vital for improving treatment outcomes[13].

1.7 Measure Breast Tumors size:

The main breast cancer tumor is measured at its broadest position by physicians. The size is typically expressed in millimeters (mm) or centimeters (cm). **TX:** The physician is unable to assess the primary tumor.

- **T0:** The physician has not found evidence of a primary tumor.
- **T1:** The tumor is 2 cm (0.79 inches) or less in diameter.
- **T2:** The tumor is more than 2 cm but less than 5 cm (1.97 inches) across.
- **T3:** The tumor is larger than 5 cm (1.97 inches) wide.
- **T4:** The tumor can be of any size, but it is growing into the chest wall or skin.

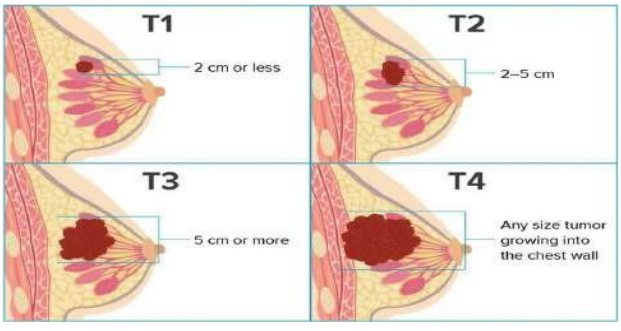

Figure 1.6 Stages are Based on Tumor Size

1.8 Stages of Breast Tumors:

Once the cancer is diagnosed, a critical step is to determine its stage, which is indicative of its level of advancement. The appropriate treatment for specific case staging plays a vital role. This assessment considers various factors, with tumor size being a significant determinant in the staging of breast cancer.

In the staging process, the **TNM** (Tumor, Node and Metastasis) staging system values are commonly utilized to categorize and diagnose breast tumors accurately. These values provide a comprehensive picture of the extent of the tumor within the breast and its potential to spread to nearby lymph nodes or distant sites. This information guides healthcare professionals in developing a tailored treatment plan based on the specific stage of breast cancer[14]. **TNM** stands for:

- **T** is the major or primary tumor size.
- **N** is if cancer spreads to neighboring lymph nodes.
- **M** is a metastasis, meaning cancer has spread to other body parts.

Breast cancer stages depend on the size and type of tumor. The stages used to study cancer are numbered from 0 to 4 (0. I. II. III. IV). Breast cancer in stage 0 is still in its initial stages and has not spread. Stage 4 breast cancer is last stage cancer that has spread to certain other parts of the body.

Stage 0:

This is for explanation and understanding non-invasive breast cancers, such as Ductal Carcinoma in Situ (DCIS). It remains in the area or region of origin. It has no effects on other parts of the body and does not impact on their smooth function. It remains in the area or region of origin. The 5-year survival rate* is 98%.

Stage I:

This is related to invasive breast cancer, that is, it spreads to other regions around the affected breast. The tumor measures up to 2 centimeters, but it has not yet spread outside the breast. The 5-year survival rate* is 85%.

Stage II:

At this stage, the tumor measures between 2 to 5 centimeters and gradually affects

the axillary lymph nodes. A biopsy is needed for detection. The 5-year survival rate* is 55%.

Stage III:

The tumor has increased in size and spread to adjoining regions such as the underarms and the breastbone. The 5-year survival rate* is 55%.

Stage IV:

Spreading to areas other than the breast, cancer reaches and impacts other body parts as well which then fail to perform their functions and eventually the body stops working. The 5-year survival rate* is 10%[14], [15].

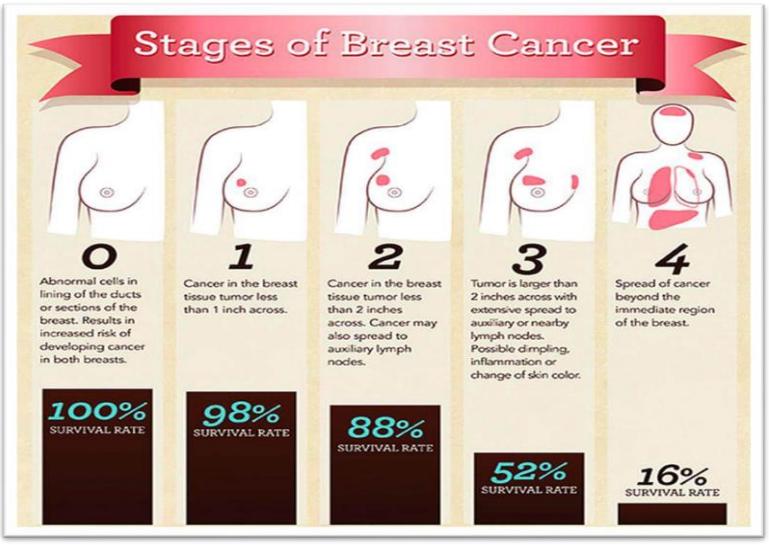

Figure 1.7 Stages of Breast Tumor

1.9 Phantom:

In a medical or scientific context, a phantom is a man-made object designed to simulate the structure and characteristics of human tissue or organs, or the entire body for use in medical research, diagnostics, imaging and therapy. Phantoms are well employed in the field of radiology, radiation therapy, nuclear medicine, and in medical physics. It substitutes human tissue in experimentation to assist healthcare professionals and researchers on how to develop, test, and calibrate medical imaging devices (CT, MRI, PET or ultrasound) and equipment for radiation therapy. In the training of healthcare professionals, as well as in the development of new diagnostic and treatment techniques, phantoms play the critical role because they wipe out the need to expose real patients to potentially harmful procedures during the testing phase. We can

synthesize phantoms from a variety of materials, including gels, plastics, silicones, and polymers[16].

To match the density, atomic composition, acoustic properties, and radiological behavior of real human tissues these materials are selected and modified. For example, in the field of radiation therapy, the model (phantom) of muscle or bone should resemble the same density and X-ray absorption properties, so it should respond as natural tissue when interacting with the radiation beams. This makes sure the exact simulation of dose delivery, scattering, and absorption[17]

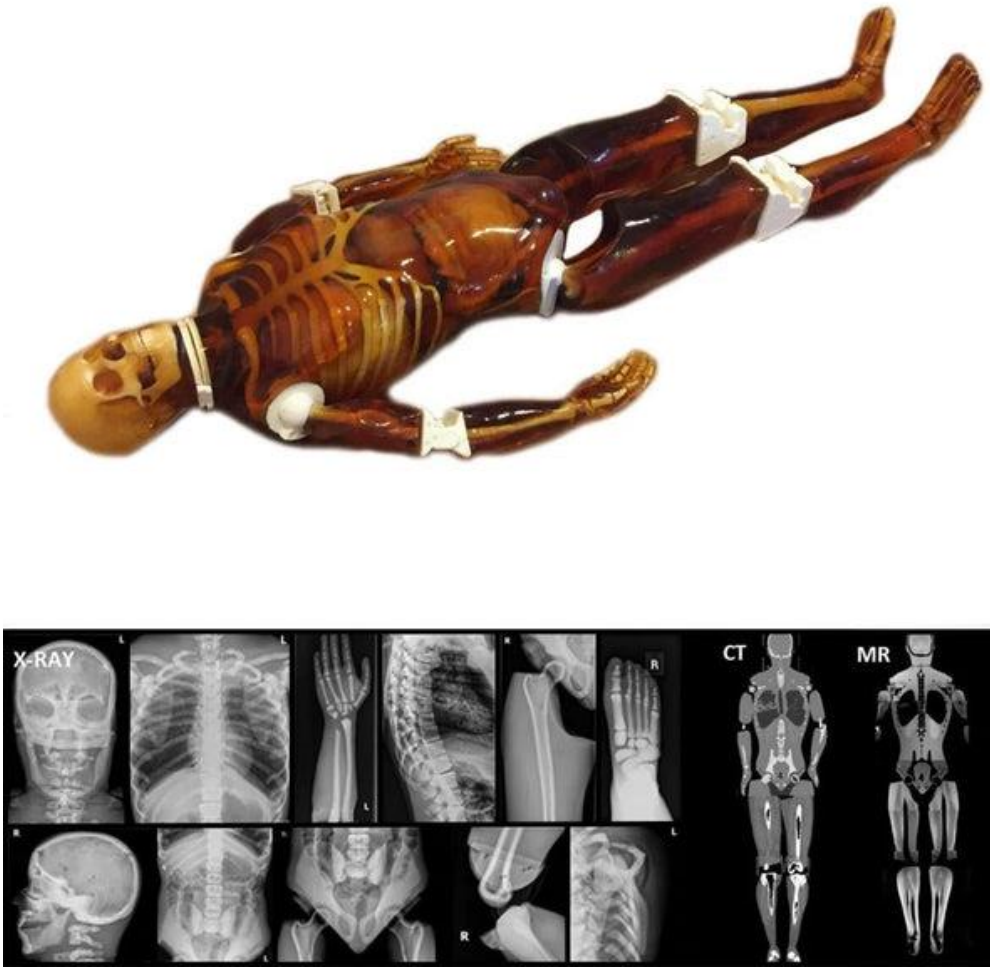

Figure 1.8 Anthropomorphic liver phantom for liver therapy research and training

1.10 Importance of Phantom:

Tissue-equivalent phantoms are vital tools for the precise detection of breast cancer. By mimicking the physical and anatomical characteristics of real breast tissue such as density, atomic composition, and radiation absorption these models enable medical physicists to calibrate imaging devices and confirm diagnostic techniques with

exceedingly precise results. In diagnostic imaging, phantoms help the evaluation and enhancement of the image quality, contrast, and spatial resolution, which are crucial for identifying tiny or early-stage malignancies. They are also involved in developing and testing new approaches to imaging and launching treatments. Especially, these phantoms can be uniquely made to represent tissues or organs, giving them great value in specialized testing and experimentation.

These phantoms provide an appropriate and controlled environment in which medical professionals may practice imaging techniques without exposing patients to risk. They are also used to evaluate and improve different types of imaging such as mammography, ultrasound, MRI, and CT, making sure that these systems can detect even tiny variations in breast tissue. Phantoms help in the evaluation of tumor identification and the comparison of various diagnostic procedures by replicating real-world medical conditions.

Furthermore, phantoms may be modified to represent certain tissues or tumor characteristics, which are very useful in breast cancer research and testing. They contribute to the creation of novel diagnostic techniques, imaging technologies, and nanoparticle contrast enhancement. Phantoms enable researchers to identify technological errors, dislocations and boundaries before using a novel diagnostic procedure on actual patients, improving accuracy and patient safety. Finally, tissue-equivalent phantoms contribute significantly to the reliability, safety, and accuracy of breast cancer detection. They ensure imaging systems are appropriately calibrated, medically examined, and capable of providing patient-specific diagnostic information, making them crucial to advanced breast cancer diagnosis and research[18].

1.11 Types of Phantoms:

Depending on their internal structure, characteristics and composition phantoms are categorized into **homogeneous** and **heterogeneous** phantoms.

1.11.1 Homogeneous phantoms:

Homogeneous phantoms are made entirely from a material which retains the same properties throughout. Such items generally have simple shapes such as cubes or cylinders and are used mainly for the basic calibration, dosimetry check and quality control. A disadvantage of homogenous phantoms is that they do not represent human tissue structure correctly.

1.11.2 Heterogeneous phantoms:

Heterogeneous (anthropomorphic) phantoms mimic the inhomogeneous composition of tissue. These, often shaped like specific human body parts thus, provide more anatomically realistic models. They contain multiple layers synthesized from tissue-equivalent materials that mimic different human tissues (skin, fat, muscle, bone, tumors). For example, breast phantoms with distinct skin, adipose, glandular and tumor regions[19].

1.12 Phantoms for Diagnosis:

Tissue-equivalent breast phantoms are important in radiation dosimetry and imaging precision for diagnosing breast cancer. These phantoms are used to monitor and estimate the absorbed dosage of ionizing radiation in breast tissues and tumor locations, allowing for safe and reliable diagnostic imaging. They are made from water-equivalent or tissue-equivalent materials that closely mimic the anatomical structure and radiological characteristics of natural human breast tumor tissue.

Phantom materials in breast imaging are meant to mimic the physical features of tumor tissue, allowing imaging systems such as mammography, CT, MRI, PET, and ultrasound to be accurately evaluated and examined. This enhances picture quality, contrast, tumor visibility, and tissue damage detectability, which are crucial for the early and precise identification of breast cancer. In phantom fabrication, fundamental characteristics like X-ray attenuation, scattering, density, elasticity, and biological geometry may be precisely maintained[20].

This allows researchers and medical physicists to evaluate the ability for imaging systems to identify and distinguish tumor tissue from surrounding healthy tissue, so ensuring that diagnostic techniques maintain high accuracy with minimal radiation exposure. Frequently used breast phantoms contain gel-based phantoms, polymer phantoms, solid tissue phantoms, and liquid phantoms, typically merged with mimicked nodules for tumors to represent genuine medical situations. These phantoms offer realistic environments for testing and help improve diagnostic approaches for breast cancer detection, localization, and image quality analysis.

Tissue-equivalent phantoms are critical tools in modern medical physics, providing a reliable and ethical way to replicate human tissue behavior under radiation. They bridge

the gap between clinical application and theoretical planning which enhance patient safety and improve treatment outcomes[21], [22].

1.13 Breast tissue Phantom:

Phantoms are a vital element of medical imaging systems used for accurate evaluation, radiation dosage analysis and performance optimization in the diagnosis of breast cancer. A breast phantom is a type of anthropomorphic phantom synthesized to mimic the radiological properties and anatomy of the real human breast. It is broadly used in the examining of breast imaging techniques like mammography, ultrasound, MRI, and computed tomography (CT), as well as in radiotherapy planning for breast cancer treatment. There are various tissue-mimicking materials in the breast tissues. Using water-soluble components such as Agar and Gelatin as a source of fats and water led to the realistic tissue composition of the breast. In modern medicine, phantoms are essential tools and the breast phantom is a specialized edition that allows clinicians and researchers to study imaging and therapeutic methods for breast tissue in a highly controlled and reproducible way which ultimately helps to improve treatment and early detection of breast cancer[23].

1.14 Requirements for realistic Breast Phantom:

A realistic Breast Phantom shows effective results for estimating radiation dose in cancer treatment. For a realistic phantom following are requirements:

1. Phantoms should contain fat-water percentages of different layers of the breast. The amount of fat and water differentiate between the healthy and tumor tissue in the breast.
2. Phantoms should be made so they can be cut with an electrosurgical knife. During electro surgery, alternating current is used to ionize molecules in the tumor tissue, so Phantom should have sufficient electrical conductivity like real tissues.
3. For X-ray, CT, MRI or ultrasound compatibility the materials used must match the mass density, electron density, and attenuation coefficients of actual breast tissues.
4. Especially for ultrasound and compression mammography studies the synthesized phantom should have soft tissue-like elasticity and compressibility, like the real human breast.
5. Phantoms should not be exposed to high temperatures.
6. For different simulation purposes like radiation therapy, a phantom should be

shaped similarly to the breast tissue or tumor.

7. It should be easily manufactured, shaped, and not degrade quickly over time[20], [24].

1.15 Breast Tumor treatments:

There are several types and procedures of cancer tumor treatments and follow-ups according to tumor size, type, and stage.

1) Chemotherapy
2) Radiation Therapy
3) Surgery
4) High Beam Radiation
5) External Beam Radiotherapy

One of the most frequent questions in medical treatment is about how imaging and radiation-based approaches help with breast cancer diagnosis. Diagnostic technologies such as mammography, ultrasound, MRI, PET/CT, and digital breast biopsy have distinct benefits that can be more successful than traditional medical screening individually. The most significant benefit of these imaging modalities is their abilities to detect tumors at an early stage with high precision, detect microcalcifications, determine tumor size, and differentiate between benign and malignant tissues.

In current diagnostic practice, accuracy, sensitivity, and least extent of penetration are essential and radiation-based imaging methods can provide these characteristics. When several imaging methods are combined, such as mammography and ultrasound or MRI, the chances of early cancer diagnosis increase substantially, minimizing error rates and improving the outcomes for patients. These methodologies help in tumor localization, biopsy treatment direction and disease progression estimation, and are frequently more reliable and less capable of shortcomings compared to invasive diagnostic techniques[25].

1.16 Nanoparticles in the Diagnosis of Cancer:

Over the past few years, nanotechnology has opened new horizons in the diagnosis and treatment of cancer. Metal oxide nanoparticles are different from other classes of nanomaterials and have received special attention because of their fine physicochemical properties, biocompatibility, and therapeutic potential. Nanoparticles are an advanced

diagnostic tool that helps in early tumor detection, accurate modeling, and improved division between normal and malignant tissues, making them extremely useful for breast cancer diagnostics research employing phantom-based models. Researchers are still examining the application of metal nanoparticles as contrast agents for MRI, CT, optical and imaging[26], [27].

1.16.1 Nanoparticles for Medical Imaging:

Medical imaging is frequently used for observing the progression of diseases, identify abnormalities, and examining biological processes. The advancement of cutting-edge imaging technology is constantly improving the clarity of medical images. Magnetic resonance imaging (MRI) computed tomography (CT), positron emission tomography (PET), optical fluorescence imaging, photoacoustic imaging (PA), single-photon emission computed tomography (SPECT), and ultrasound imaging are some of these techniques.

Imaging methods are essential to the diagnosis and treatment of cancer. The magnetic, optical, acoustic, and structural characteristics of several NPs, including iron oxide NPs, can improve imaging. According to previous studies, introducing NPs into target tissues can enhance contrast and image guidance for tumor detection and removal[28].

Chapter 2 Literature Review

1. **Selma et al.** has reported that Ag_2O nanoparticles (NPs) can be synthesized via a straightforward chemical co-precipitation method using silver nitrate ($AgNO_3$) as the silver source and a precipitating agent such as sodium hydroxide (NaOH) to induce formation of silver oxide phases. This method relies on dissolving $AgNO_3$ in aqueous media and carefully adding a base until a controlled precipitation of Ag_2O occurs, forming a solid nanoparticle product which is subsequently washed and dried. In typical co-precipitation, Ag^+ ions from silver nitrate react with hydroxide ions once the pH is increased (often by NaOH addition), causing the nucleation of Ag_2O solid precipitate. The reaction is generally conducted at moderate temperatures with constant stirring to promote uniform nucleation and particle size control. The precipitated Ag_2O NPs are then collected by filtration, thoroughly washed to remove unreacted reagents, and dried prior to characterization. Control over pH, deposition rate of NaOH, and reaction time can significantly influence particle size, crystallinity, and morphology. Characterization of co-precipitated Ag_2O nanoparticles typically demonstrates a cubic crystalline phase consistent with silver oxide structures. Techniques such as X-ray diffraction (XRD) confirm phase purity and crystallite size, while scanning electron microscopy (SEM) reveal predominantly spherical or near-spherical morphologies with sizes often ranging from tens to a few hundred nanometers depending on synthesis conditions and any stabilizing agents present[29].
2. **Asif et al. (2024)** investigated the synthesis, characterization, and biomedical potential of silver oxide (Ag_2O) nanoparticles prepared via chemical and green synthesis routes to evaluate their anticancer and antiviral activities. Silver nitrate was used as the metal precursor, and Ag_2O nanoparticles were formed through controlled precipitation, followed by purification and drying. The synthesized nanoparticles were thoroughly characterized using X-ray diffraction (XRD), UV–visible spectroscopy, and scanning electron microscopy (SEM), which confirmed the successful formation of crystalline Ag_2O nanoparticles with predominantly spherical morphology and nanoscale dimensions. Optical analysis revealed characteristic absorption features associated with Ag_2O formation, while morphological studies demonstrated relatively uniform particle distribution. Biological evaluation was conducted using the MCF-7 human breast cancer cell

line, where both chemically and green-synthesized Ag_2O nanoparticles exhibited dose-dependent cytotoxic effects, attributed primarily to oxidative stress and disruption of cellular metabolism. Notably, green-synthesized Ag_2O nanoparticles showed enhanced anticancer efficacy, reflected by lower IC_{50} values compared to chemically synthesized counterparts, indicating the influence of surface chemistry and bioactive capping agents on cellular interactions. In addition to anticancer activity, the nanoparticles demonstrated antiviral potential, highlighting their multifunctional biomedical applicability. The authors concluded that Ag_2O nanoparticles possess significant promise as cost-effective and versatile nanomaterials for cancer-related biomedical applications, and their tunable physicochemical properties make them suitable candidates for further exploration in diagnostic imaging, therapeutic enhancement, and nanoparticle-based phantom studies[30].

3. **Ansar et al. (2019)** developed, and test soft tissue phantoms based on silicone rubber (RTV-52), room-temperature vulcanized, with glycerin at different concentrations as an additive. Their work was motivated by the need to create a long-lasting, biologically relevant phantom material that could emulate mechanics and chemistry of human soft tissue, in particular liver tissue. Thirteen formulations in total were manufactured with 0%, 10%, 20%, 30%, and 40% glycerin and based on the physical continuity of specimens, resistance to fungi, chemical interactions by Fourier Transform Infra-red (FTIR) spectroscopy and change mechanical resistance that tested by the elastic module. It was found that samples containing 20% or less glycerin had good dispersion, good dimensional stability and less rough edge of material particles, but samples containing 30 % or 40 % glycerin were uneven, and there were visible glycerin deposits and poor miscibility. The FTIR suggested the presence of characteristic functional groups of poly (dimethyl siloxane) (Si–CH_3) at 1261 and 802 cm^{-1} and Si–O–Si siloxane bond at 1024 cm^{-1} in all the glycerin concentration cases. The enhancement of the absorption intensity of hydroxyl (–OH) groups with the addition of glycerin at 3412 cm^{-1} and 1320 cm^{-1}, which corresponds to enhanced hydrophilic property, was helpful to mimic the tissue water content. The elastic modulus was reduced from 244 kPa in the 0% glycerin sample to 126 kPa in the 20% glycerin samples, which is within the range of human liver tissue elasticity (from 0.6 to 4000 kPa). Furthermore, degradation tests showed that the phantoms were stable (did not support fungal growth) like

some of the gelatin-based alternatives described in previous literature, exemplifying further the strength of silicone rubber material. Overall, the study identified RTV silicone rubber as a promising material for phantoms and one in which moldable, long 26 life and biologically relevant physical and chemical characteristics can be developed, 10–20% glycerin being the optimal mixture for maintaining structural integrity and biological mimicry[31].

4. **Anugrah et al. (2021)** studied composites for breast phantom with combinations of gelatin, polyvinyl alcohol and some inorganic fillers such as Zn, ZnO, CuO, Co $(NO_3)_2$ and Fe_2O_3, to demonstrate their structural, mechanical and radiological characteristics for the purpose of X-ray imaging and radiation dosimetry. In this study, the importance of the phantom material to be such that is close to the properties of human tissue for elasticity, water absorption and X ray interaction properties was underlined. The phantoms were fabricated with the gel-casting technique by casting the mixture of gelatin and PVA as well as metal additives, and the obtained mixture was molded to form solid samples, then cooled in a refrigerator. Material characterization showed that the gelatin/PVA/Zn composite leaded the group, in terms of linear attenuation coefficient (0.343 cm^{-1} at 60 keV), like the theoretical value of attenuation in breast tissue, indicating its promising radiation absorption efficiency. Analysis by FTIR confirmed the presence of O–H, C–H and C=O functional groups that facilitate covalent bonding between the matrix and fillers, while XRD results revealed significant dependence of crystallite size, porosity and dislocation density on the type of fillers: samples based on Zn contained small crystals and with a high degree of porosity that were promising owing to their properties of interaction with the radiation. The swelling, the mechanical properties (tensile strength, Young's modulus, elongation at break), and the density measurements highlighted the ability of composites containing Zn and ZnO particles to provide the necessary elasticity and strength to the composites by reinforcing the interfacial interactions between the polymer matrix and the particles. In addition, the quantitative radiation absorption analysis such as photoelectric effect, atomic cross section, and electronic cross section demonstrated good agreement with experimental X-ray data and XCOM database. It is noteworthy that although gelatin/PVA/Zn composite exhibited excellent absorption and mechanical properties, the highest electronic and atomic properties ascribed to breast tissue compatibility, and thus it was the most promising among the ones investigated. The

gelatin/PVA/Zn formula 27 may be a promising tissue equivalent/pseudo human phantom as a low-cost material for diagnostic imaging and radiation treatment beam dosimetry[32].

5. **Di Meo et al. (2023)** proposed a multi-layer breast phantom with a structured fabrication process for microwave and millimeter wave imaging specifically based on preserving homogeneous dielectric properties throughout a heterogeneous design. The goal was to simulate normal and neoplastic breast tissues with oil and gelatin mixtures validated in previous studies, and to measure their EM properties from 0.5 to 40 GHz. The mixtures used by the researchers included the G_5O_{50} representing healthy tissue and G_8O_{20} representing a malignant inclusion, containing an emulsion with exact oil, water, detergent, and gelatin contents to represent realistic tissue interfaces. Planar and conformal layered phantoms were fabricated using a two-step molding procedure. This process involved serial freezing and layering to embed tumor-like inclusions in a healthy tissue matrix and to ensure homogeneous solidification and adherence between the layers. Most importantly, the dielectric measurements post-solidification showed that the cooling and layering process did not change the dielectric property invoked in the mix, thus validating its stability for imaging purposes. The convenience and simplicity of using nontoxic, readily available materials and the lack of dependence on sophisticated processing techniques such as 3D printing was a clear advantage. The characterization of these phantoms was performed using a Keysight E5063A ENA Series Network Analyzer and dielectric probe setup, and the measurements were found to be comparable to previously reported values in the literature, thus validating the reliability of the material platform. The work adds to the array of diagnostic phantoms by providing a practical method to create multi layered breast models that possess realistic attenuation, reflection, and dielectric profiling and are economically viable for electromagnetic based cancer detection[33].
6. **Anugrah et al. (2020)** Fabricated and characterized a composite soft tissue phantom comprising Ribolite/Gel wax, polyvinyl alcohol (PVA) and Rhizophora spp particle board for radiological applications, in particular, liver phantom modelling. Four phantom variants (using gelatin contents of 16%, 20%, 24% and 28%) were developed in the study using PVA as a binder and Rhizophora particles as reinforcement. Overall characterization was comprised of physical (swelling ratio, density), chemical (FTIR, XRF), and radiological (linear and mass attenuation

coefficients, CT numbers, Half Value Layer, Mean Free Path) inspections. FTIR spectra indicated major functional groups such as O–H, C–H, Si–O, C=O, C–O, and the increasing intensity of the O–H and C=O bonds at higher gelatin contents, which suggested stronger cross-linking and binding with the particleboard network. XRF measurements showed the presence of CaO especially in samples with the higher function of gelatin, confirming the source of bone material and providing high X-ray absorption as well. Radiologically, the 20% gelatin composite showed the greatest mass attenuation coefficient (0.268 cm^2/g) and linear attenuation coefficient (0.238 cm-1), closer to the previous human liver tissue values. CT number 30 measurements also supported tissue equivalency with the average HU values recorded being between +70 to +85 HU, which corresponds to the soft tissue category. The swelling ratio measurements revealed a fast absorption of water and saturation in 1 h with less swelling in higher density composites. HVLs and MFPs varied slightly with gelatin concentrations, while the 20% gelatin phantom demonstrated the most adequate attenuation depth at HVL = 2.911 cm, the same as other studies for liver phantoms. In general, the study yielded validation of the composite's mechanical and radiological similarity to soft tissue, with Rhizophora particleboard established as a unique biodegradable reinforcing material that adds structural strength and radiological performance to budget-level phantom design[34].

7. **Slanina et al. (2022)** developed and characterized novel agar–oil–glycerin tissue-mimicking breast phantoms to study the temperature-dependent dielectric properties relevant for ultra-wideband (UWB) microwave breast tumor detection. The study was motivated by the higher water content of malignant tissue, which causes tumor permittivity to change differently with temperature compared to surrounding healthy tissue. Dielectric measurements were performed from 50 MHz to 20 GHz over a temperature range of 25–46 °C using an open-ended coaxial probe. Phantoms representing tumor, glandular tissue, skin, and fat showed distinct and reproducible temperature-dependent variations in both the real and imaginary parts of permittivity. These trends were found to qualitatively agree with measurements from porcine skin and fat tissues, validating the biological relevance of the phantoms. The results demonstrate that thermal-differential microwave imaging, particularly near physiological temperatures (~36 °C), can enhance tumor contrast without the use of external contrast agents, highlighting the potential of

temperature-based dielectric contrast for next-generation microwave breast cancer diagnostics[35].

8. **M. K. Sharma et al. (2023)** proposes a noninvasive microwave multielement sensor for analyzing breast phantoms and detecting tumors by leveraging differences in the electromagnetic responses of healthy and malignant tissues. The sensor consists of a compact array of microwave elements designed to transmit and receive signals across breast-mimicking phantoms; variations in the scattered microwave measurements are used to identify the presence of tumor-like inclusions. Experimental validation on engineered breast phantoms demonstrates the sensor's capability to distinguish normal tissue from tumor-containing regions, highlighting its potential as a low-cost, radiation-free tool for early breast tumor detection in clinical diagnostics[36].
9. **Ponsanti K et al. (2022)** reported the synthesis of hybrid mesoporous silica nanoparticles (MSNs) decorated with silver nanoparticles (AgNPs) as a promising platform for breast cancer cell detection. MSNs were synthesized to provide a high surface area, tunable pore size, and excellent biocompatibility, while AgNPs were incorporated to enhance optical and biological activity. The formation of MSN/AgNP nanocomposites was confirmed using structural and morphological characterization techniques such as XRD, FTIR, SEM/TEM, and UV–Vis's spectroscopy. The presence of AgNPs significantly improved the nanoparticles' interaction with cancer cells due to their unique plasmonic and surface properties. In vitro studies demonstrated enhanced affinity and sensitivity of the hybrid nanoparticles toward breast cancer cells compared to bare MSNs. The mesoporous structure facilitated effective nanoparticle dispersion and cellular uptake. The combined properties of MSNs and AgNPs enabled improved detection capability through optical signal enhancement. Overall, the results indicate that MSN/AgNP hybrid nanomaterials offer a stable, sensitive, and effective approach for breast cancer cell detection, with strong potential for future diagnostic and biomedical applications[37].

Chapter 3 Materials and Methods

3.1 Silver Nitrate:

To make silver nanoparticles, silver nitrate, a white, crystalline solid, provides a reliable source of Ag^+ ions. Ag ions dissolve rapidly because they are very soluble in water[38].

Figure 3.1 Silver Nitrate

3.1.1 Role in Nanoparticle Fabrication:

Because silver nitrate ($AgNO_3$) produces Ag^+ ions uniformly in solution and is very soluble in water, it is employed as the silver precursor in the production of nanoparticles. Silver oxide nanoparticles are created when Ag^+ ions combine with hydroxide ions from the precipitating agent during the co-precipitation process. The nucleation rate, particle size, and production of the nanoparticles are all regulated by the $AgNO_3$ concentration. Its high chemical purity guarantees low contaminants and repeatable synthesis. Because of their high atomic number and electron density, the resulting silver-based nanoparticles can be used to improve X-ray attenuation in CT-based breast phantom studies[39].

3.1.2 Sodium Hydroxide

A powerful inorganic base, sodium hydroxide entirely separates into Na^+ and OH^- ions and is very soluble in water. Strong alkaline qualities and significant chemical reactivity characterize this whitish, odorless, hygroscopic solid. NaOH is useful for precipitation and pH-controlled processes because it easily raises the pH of aqueous solutions. Sodium hydroxide is frequently used as a stable precipitating agent in chemical synthesis, including the formation of nanoparticles, because of its excellent purity and reactivity[40].

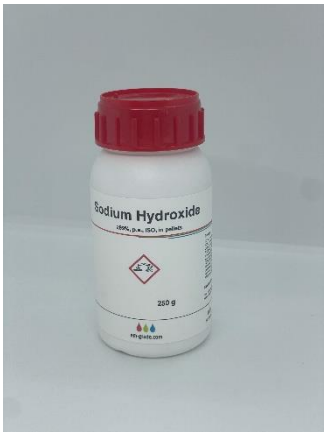

Figure 3.2 Sodium Hydroxide

3.1.3 Role in Nanoparticle Fabrication:

By adding hydroxide (OH^-) ions to the reaction solution, sodium hydroxide (NaOH) acts as the precipitating agent in the production of silver-based nanoparticles. Silver hydroxide is formed when these OH^- ions combine with Ag^+ ions from silver nitrate. This then transforms into silver oxide (Ag_2O) nanoparticles. Particle size and shape are influenced by the regulated addition of NaOH, which also controls the nucleation rate and particle development. NaOH additionally changes the solution's pH, which promotes effective precipitation and a higher yield of silver oxide nanoparticles.

3.1.4 Synthesis of Silver Oxide Nanoparticles

The co-precipitation approach was used to produce silver oxide (Ag_2O) nanoparticles because it is easy to use, repeatable, and suitable in developing fine particles at low temperatures. The reaction temperature was maintained at 80 °C while an aqueous solution of silver nitrate ($AgNO_3$) was produced in 250 mL of deionized water and continuously stirring at 250 rpm. Ag^+ and OH^- ions mixed to generate a black precipitate when a separately prepared sodium hydroxide (NaOH) solution was added dropwise to the silver nitrate solution. Uniform nucleation and development of silver oxide nanoparticles were facilitated by the controlled addition of the precipitating agent and the increased temperature. After collecting the precipitate using vacuum filtration with a Büchner funnel, any remaining ionic byproducts were completely cleaned up with deionized water[41]. After that, the powder was dried at 70 to 80 degrees Celsius in an oven to remove moist while maintaining the oxide phase. Because silver has a high atomic number (Z = 47) and a high electron density, which greatly improves X-ray attenuation, silver oxide nanoparticles are very useful for computed tomography (CT) imaging applications. Ag2O nanoparticles improve cancer identification and brightness-to-noise ratio when inserted in a breast phantom by increasing imaging contrast in comparison to surrounding soft-tissue-equivalent components. The use of silver-based nanoparticles in breast phantoms offers a reliable foundation for researching nanoparticle-enhanced diagnostic methods for the detection of breast cancer and enables controlled evaluation of CT imaging performance[42].

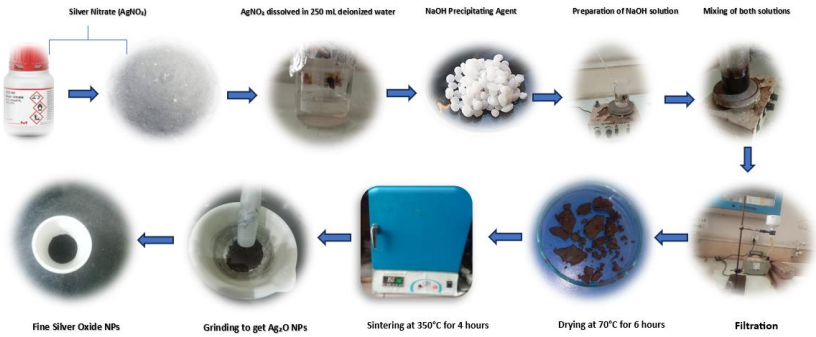

Figure 3.3 Synthesis of Silver Oxide Nanoparticles

3.2 Iron (III) Nitrate Nonahydrate:

Iron (III) Nitrate Nonahydrate [$Fe(NO_3)_3 \cdot 9H_2O$] is a yellow-to-pale brown solid that is utilized as a primary Fe precursor to make iron oxide nanoparticles. It is the source of Fe^{3+} ions in chemical processes and is highly soluble in water and other organic solvents. When it comes to its aqueous solution, $Fe(NO_3)_3 \cdot 9H_2O$ is very reactive and hydrolyzes. For the sol gel synthesis of magnetite (Fe_3O_4) and other iron-containing nanoparticles, it provides a reliable and effective source for iron nanoparticles. During the process of crystal formation, it encourages nucleation and growth. As an effective iron precursor for diagnostic applications, it is crucial to the production of nanoparticles[43].

Figure 3.4 Iron Nitrate

3.2.1 Role in Nanoparticle Fabrication:

Fe_3O_4 was used as the iron source for Sol Gel production of $Fe(NO_3)_3 \cdot 9H_2O$ NPs. Because of its superior solubility and accessibility of the Fe^{3+}-ion, the nucleation and growth of the Fe oxide crystals on the surface remained homogeneous throughout the gelation stage, resulting in a stable nanoparticle structure[44].

3.2.2 Citric Acid

Citric acid is a weak organic tricarboxylic acid that has an immense capacity to chelate metal ions and is very soluble in water. It's one hydroxyl (–OH) group and three carboxyl (–COOH) groups allow for efficient interaction with Fe^{3+} ions for producing stable metal–citrate complexes. Citric acid serves as a chelating and polymerizing agent

in sol-gel production, stimulating uniform ion distribution and regulated particle synthesis. Additionally, it minimizes the formation of aggregates of nanoparticles and helps avoid early precipitation. Furthermore, phase-pure metal oxide nanoparticles are facilitated by the clean hydrolysis of citric acid during heat treatment[45].

3.2.3 Role in Nanoparticle Fabrication:

As a chelating and integrating agent that binds metal ions and maintains their uniform distribution in solution, citric acid is essential to the synthesis of nanoparticles. It reduces agglomeration and improves particle size efficiency by controlling nucleation and growth. Citric acid promotes the creation of polymeric networks during the sol-gel process. It dissolves when heated, which enables the synthesis of crystalline, pure metal oxide nanoparticles[46].

3.2.4 Synthesis of Iron Oxide Nanoparticles

Iron nitrate was used as the metal precursor and citric acid as the chelating agent in the sol-gel process for production of iron oxide nanoparticles. To create a clear, uniform solution, 11.8 g of iron nitrate was measured and dissolved in deionized water while being constantly stirred. A porous chelating solution was created by dissolving 13.22 g of citric acid in deionized water. The iron nitrate solution was continuously stirred while the citric acid solution was added dropwise. Citric acid successfully chelated Fe^{3+} ions throughout this process, yielding a stable metal–citrate complex that guaranteed even distribution of iron ions at the molecular level[47].

Steady solvent evaporation was made feasible by controlled heating and constant stirring, producing a viscous sol that later changed into a homogenous gel. To eliminate any remaining moisture, volatile ingredients and create a dry precursor, the resulting gel was dried in an oven at 130 °C for seven hours. The organic matrix was thermally broken down, and iron oxide nanoparticles were crystallized after the dry material was sintered at 350 °C for five hours. The sintered product was partially grounded after cooling to room temperature to provide uniform iron oxide nano powder that could be used in breast phantom applications and further characterized[48].

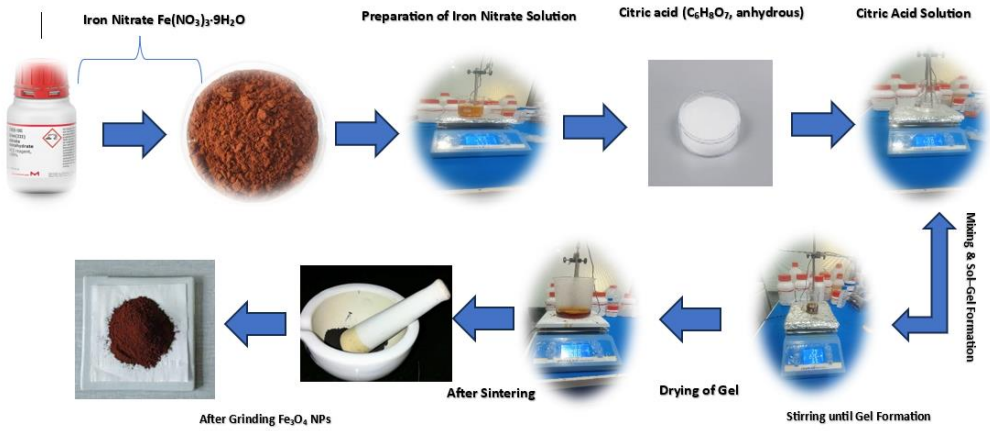

Figure 3.5 Synthesis of Iron Oxide Nanoparticles

3.3 Preparation and methodology of Homogeneous Breast Phantom:

Tumor tissue was integrated with the tissue-mimicking layer to create a homogenous breast tumor phantom. That layer was created using a separately prepared solution at a controlled temperature while being continuously stirred magnetically for a specific period. It was suitable for homogenous material and repeatable for phantom structures[49]. This tissue-mimicking layer was created utilizing optimal compositions to replicate the mechanical and diagnostic 3characteristics of actual breast tissue.

3.3.1 Gelatin:

A naturally occurring water-soluble protein, gelatin is produced when collagen is partially hydrolyzed. Bones, animal pelts, and fish head skin are rich sources of the collagen. Proline makes up over 22.5% of collagen, a high molecular weight protein with a repeating amino acid sequence. Collagen is broken down to yield gelatin, a material with a wide range of potential uses in food and medicine due to its biocompatibility. A few physicochemical characteristics are responsible for their gel-forming capacity[50].

Figure 3.6 Gelatin

3.3.1.1 Gelatin is used in making phantoms:

I chose gelatin as the basic material for our breast tissue phantom because it most closely follows the protein composition of natural human breast tissue. It has the softness and elasticity of biological tissues, taking all these factors into account: one's slope. Furthermore, its gel-forming action allows stable, isotropic layers to be produced which are essential for constructing realistic tissue properties in radiation therapy research[51].

3.3.2 Sodium chloride NaCl:

Figure 3.7 NaCl

The common chemical equation for sodium chloride is NaCl, but most people refer do it as table salt. This compound consists of sodium (Na+) and chloride ions (Cl-) with 1:1 ratio. It is a natural, abundant and fully essential biological electrolyte that may be employed for numerous industrial, chemical and biomedical purposes. It is found in sea water and mineral deposits; it dissolves easily in water. NaCl table salt, is a crystal solid and it provides a good example of the thermal and chemical stability of this class of compounds. The other important role of sodium chloride for the ionic strength of solutions also affects how charged biomolecules and substances will act in the solution. In the fields of biomedical and physiology, sodium chloride is essential for maintaining the homeostasis of the cell, for the conduction of nerve impulses, and for normal muscle performance.

3.3.3 Polyvinyl alcohol (PVA):

Figure 3.8 Polyvinyl Alcohol

Polyvinyl alcohol (PVA) is a water-soluble synthetic polymer derived from the hydrolysis of polyvinyl acetate. It is a biocompatible non-toxic material that is extensively used in biomedicine, pharmacology and industry. It is an excellent additive for use in water-fluid-system hydrogels and as a mimic material of biological tissue. PVA exhibits high tensile strength, flexibility, and stability in an aqueous medium. PVA

also has good thermal stability, can cross-link and enhance mechanical strength and water retention in the form of networks. Due to its biocompatibility and nontoxicity, PVA has been widely used in wound dressings, contact lenses, artificial organs and drug delivery systems[52].

3.3.3.1 PVA used in making phantoms:

In fabrication of breast tissue phantom, PVA acted as reinforcement agent (owing to which it acted) such that could reinforce mechanical properties and elasticity more effectively. Its inclusion strengthened the layers in the phantom so that they would maintain their shape and consistency during handling and irradiation. Furthermore, PVA contributes in maintaining the stability of the gel framework, thus helping to maintain homogeneity of the formulation and to reduce drying throughout time. Due to its compatibility with hydrophilic and hydrophobic constituents, it was the material of choice for complex multilayer phantoms[53].

3.3.4 Glycerin:

Glycerin is a simple polyol compound, is a colorless, odorless, sweet-tasting, viscous liquid that is widely used in pharmaceutical formulations. It is a sweet-tasting, viscous liquid that is monohydric and is soluble in water. Glycerin is a natural ingredient of animal and plant lipids, and plays an important role in the pharmaceutical, cosmetic, food and biomedical industries because of its biocompatibility and its hygroscopic behavior. It has high boiling points, low vapor pressure, and does not decompose with heat. Its lubricity and viscosity lend its use to applications as a stabilizer and thickening agent. Due to its biocompatibility, glycerin can be used for tissue engineering, cell culture, and soft tissue phantoms[54].

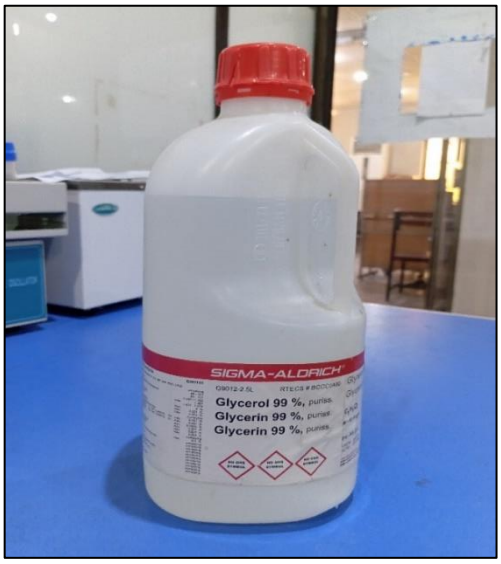

Figure 3.9 Glycerin

3.3.4.1 Glycerin is used in making phantoms:

A plasticizing and hydrating agent (glycerin) was also added in the breast tissue phantom to enhance the elasticity, softness, and water-absorption features of the gelatin gel. Its hygroscopic character allowed to minimize the dehydration during the setting process and during storage of the phantom, and its inherent plasticizing behavior made the material behave more like human breast. The presence of glycerin also increased the overall strength and the stability of the phantom layers[55].

3.3.5 Agar:

Agar is a natural polysaccharide that is mainly obtained from red algae. It consists mainly of two elements: a linear polymer that forms a gel, agarose, and a sulfated, branched polysaccharide. Furthermore, agar has been widely applied in the fields of microbiology, food industry and biomedicine as a gelling agent with good gel strength, biocompatibility and even thermal resistance properties. Agar has a good capability of gels and rapid release of carriers than makes firm stable gels even at low concentrations (1-2%). It has a melting point of approximately 85–90°C and a solidification point of 32–40°C. Agar is known for its hydrophilic, biocompatible, biodegradable, nontoxic, and chemically inert properties. With its strength, transparency and ability to hold shape over time. Agar is used in various biomedical applications, such as in tissue engineering scaffolds, drug delivery systems, and diagnostic culture media[56].

Figure 3.10 Agar

3.3.5.1 Agar used in making phantoms:

In the breast phantom, agar was used for the tumor layer to increase stiffness, structural integrity, and mass. Its introduction increased composition strength and sharpness to facilitate the differentiation from surrounding soft tissues of tumor region. Agar also contributed to the radiological difference of the tumor, increasing the phantom visibility and the realism both under imaging and irradiation. Its onset and solidification were

compatible with the gelatin and other hydrogel materials, which contributed to the homogeneous mixing and solidification process[55].

3.4 Tumor tissue preparation:

Dissolve 7g of NaCl in 20ml of DI-water under continuous stirring for 1 hour at room temperature. Separately dissolve 9g of gelatin in 60ml of DI-water under continuous stirring for 3 hours at 35 °C. Prepare the solution of 1.5g Agar in 20ml of DI-water for 1 hour at room temperature. Mix all the solutions in large beaker and add 0.5ml of formalin under continuous stirring for 2 hours. Dissolve 3ml of vegetable oil in 10ml of ethanol under constant stirring for 1 hour and add detergent and mix it for 1 hour. Mix all the above solutions in large beaker under continuous stirring at 35 °C for 3 hours. Now prepare the solution of 6.5g PEG in 32.5ml DI-water and add it in beaker during the stirring process. After stirring it for 1 hour, we will get the homogeneous solution[57].

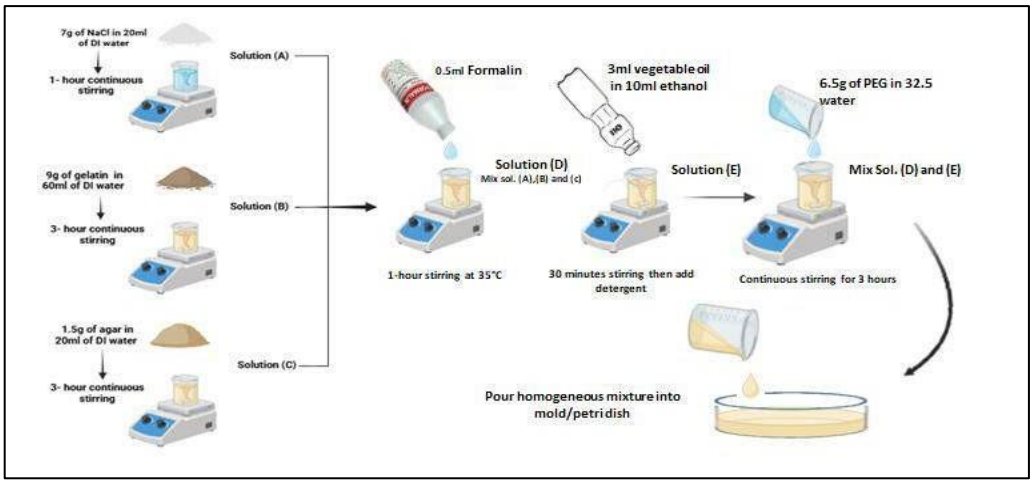

Figure 3.11 Fabrication of phantom Tissue

3.5 Embedment of nanoparticles into breast tumor phantom:

To integrate iron oxide nanoparticles into the tumor layer of the breast phantom, two distinct methods were employed:

3.5.1 Pre-mixing Method:

In this method, nanoparticles were integrated directly into the tumor gel and then allowed to solidify. 10 mL of the prepared tumor tissue solution was taken and mixed with 5 mL of the nanoparticle suspension. The resultant solution was sonicated for 20 min to prevent agglomerate of the nanoparticles with the tumor matrix. The sonication was done carefully to prevent foam formation and a homogeneous distribution of the gel within the gel-based hydrogel was retained without degrading the structural integrity of the gel[58].

3.6 Characterization Techniques:

Different characterization approaches have been explored and examined to study material characterization and analysis, as explained below:

3.6.1 Fourier Transform Infrared Spectroscopy (FTIR):

FTIR is a Fourier Transform Infrared Spectroscopy in which the brighter the infrared light interacts with material is observed across different wavelengths. FTIR visualizes gases, liquids, and solids in the items of radiation spectrums or ultraviolet. This can be non-destructive and gives information on chemical bonding in materials. It is the technique to observe the changes in the intensity of infrared light when interacting with the matter.

Figure 3.12 FTIR Machine

In most FTIR analyses, we see data in three components. The peak position comes first, then by peak width and peak intensity[59]. Every material's peak location is different thus we can tell which one it is. Peak width describes the type of functional group that bonds to the molecule, whereas peak intensity indicates the molecule's vibrational energy.

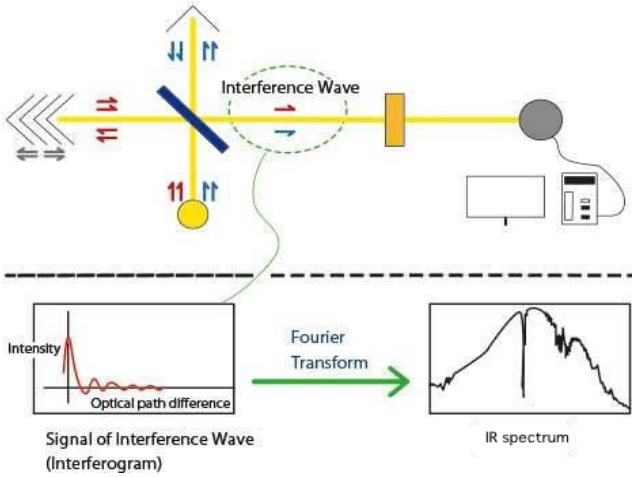

Figure 3.13 Working Principal of FTIR

3.6.2 X-ray Diffraction (XRD):

One of the most well-known techniques for material characterization is X-ray diffraction (XRD). It's determined by looking into the crystalline material's quality, crystallite size, and makeup, and structure once it's been prepared.

Figure 3.14 XRD Machine

X-rays are produced when electrons are accelerated at a high enough energy level at a metal-based target, knocking out the center electrons and energizing the electrons[60]. X rays are released when electrons from the higher shell fall into a vacancy in the lower shell. Molybdenum and copper are the most regularly utilized

metal targets. These released X rays are known as typical x-rays because their wavelengths correspond to the energy difference between two shells in a metal-based target. These typical x-rays collide with a material, scattering the x-rays[61].

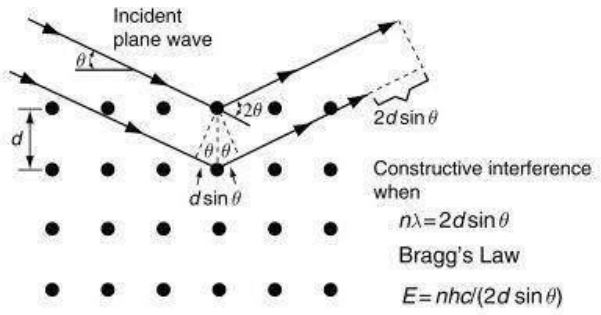

Figure 3.15 Bragg's Law

3.6.2.1 Scattering of X-Ray waves

X-ray's wavelength (1 Å -100 Å) are comparable in size to the interatomic spacing of the material, this causes the diffraction and scattering of the waves, collecting data about material-specific atoms and their arrangement. Bragg's law tells that on which wavelengths and angle's incoming incident x-ray can cause the constructive interference of dispersed waves:

$n\lambda = 2d \sin\theta$

Where, n=integer

λ = X-Rays
wavelength

d = atomic spacing
θ = angle between incident X-ray and atom layer

The full width at half of the highest value of the intensity (FWHM), which is used to measure the crystalline structural integrity, is one of the parameters that XRD can measure. Large values of FWHM describe Bragg's peaks that are wide and broad, show the amorphous shape and their crystallite size is also small[61].

The crystallite size can be measured from Scherrer's formula:

$D = 0.94л/\beta \cos\theta$

Where, D = Diameter of the grain,

β = full width at half of the maximum value of the diffraction peak (FWHM),

λ = X-ray wavelength (λ =1.54060 Å),

θ = diffraction angle at which peak

occurs, K=Scherer's constant (K =

0.94)

For a total separate protein and DNA model systems, complete and highly reliable data sets were obtained at different wavelengths between 0.80Å and 2.65Å.

3.7 Scanning Electron Microscope (SEM):

This is a high-resolution imaging method. One way of examining the surface morphology and topographical features of the materials using the micro to nanometer scale involves the use of Scanning Electron microscopy (SEM). SEM works by scanning a focused beam of high-energy electrons across the surface of a sample. These electrons will interact with the atoms of the sample generating a set of signals, such as secondary electrons, backscattered electrons and X-rays[62]. Secondary electron signal is the most popular signal in SEM; this signal occurs when the primary incident electron beam collides in elastically with the atoms on the surface, ejecting the secondary. The electrons are of low energy, and they give high-resolution images of features of the surface since their generation is limited to a shallow depth at the sample surface.

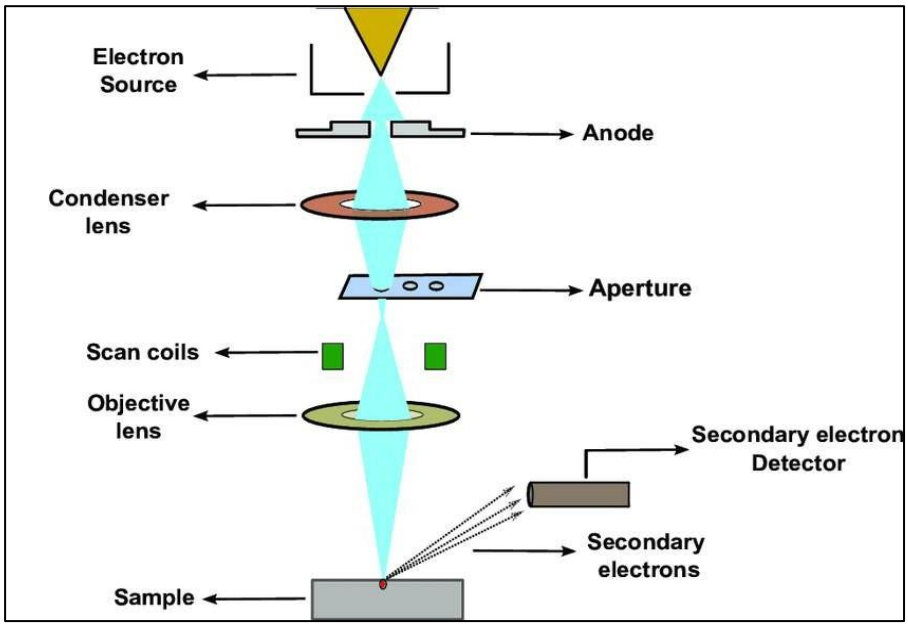

Figure 3.16 Working Principal of SEM

The electron gun creates electrons that are directed to a small beam using electromagnetic lenses. And as this beam sweeps across the sample in what is called a raster pattern, the returned signals are gathered by detectors, and the signal is used to create a detailed picture of the surface. The picture is displayed in real-time on a screen and could be zoomed-in as tiny as 10x to as large as 100,000x, varying with system. An investigation on the surface morphology of synthesized iron oxide nanoparticle was made by SEM. The SEM images confirmed the approximate shape, surface texture and agglomeration extent of the nanoparticles[63]. These results help correlate the observed particle structure with synthesis conditions, such as temperature, solvent, or stabilizer concentration.

3.8 CT scan:

A Computed Tomography **(**CT**)** scan is a diagnostic imaging technique that uses **X-**rays and computer processing to create detailed cross**-**sectional images (slices) of the body. As the X-ray tube revolves about the body multiple X-ray images are taken from different angles during a CT scan[64]. A computer processes these images to create 2D slices and 3D images of inside structure of the body. CT operates by evaluating how much the X-ray beam is absorbed or blocked by different materials inside the body. This process is called attenuation. Denser objects like bone or metal absorb more X-rays and appear brighter on the image, while less dense materials like fat or air absorb less and appear darker.

The attenuation depends on the material's density**,** atomic number (Z) and thickness**.** Each part of the image is assigned to a value called a CT number or Hounsfield Unit **(HU)**, which shows how dense that region is compared to water.

CT number calculated as:

$$\mathrm{HU} = \left(\frac{\mu_{\mathrm{tissue}} - \mu_{\mathrm{water}}}{\mu_{\mathrm{water}}} \right) \times 1000$$

Where:

- μ tissue = linear attenuation coefficient of the material.
- μ water = linear attenuation coefficient of water.

CT imaging was used to study the internal structure and X-ray attenuation properties of breast phantom layers[65].

Chapter 4 Results and Discussion

4.1 FTIR Analysis:

Fourier transform infrared spectroscopy (FTIR) was employed to obtain the FTIR spectrum of different materials used and obtained in the study. The FTIR analysis was conducted in the characterization lab of IRCBM. The provided FTIR (Fourier-transform infrared spectroscopy) graph illustrates the infrared absorption spectra of breast tissue-mimicking phantom.

4.1.1 FTIR Analysis of Tumor layer:

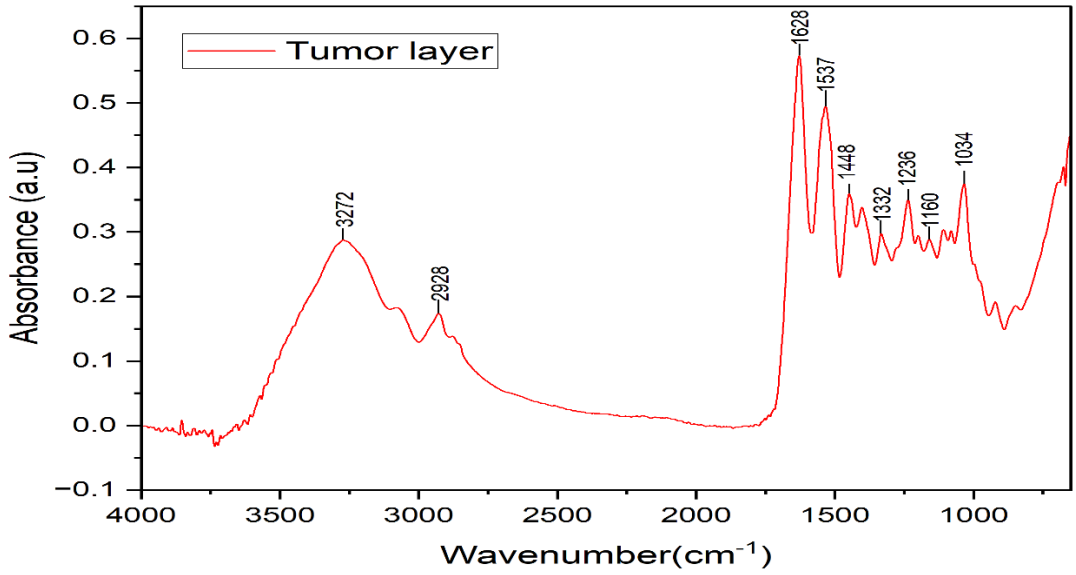

Figure 4.1 FTIR of Tumor Layer

The FTIR spectrum of tumor layer extends across wave numbers between 600 cm^{-1} to 4000 cm^{-1} The FTIR analysis proves that selected materials successfully mimic the chemical composition of real breast tissue. According to the results each group had unique absorption. A broad absorption band at **3272 cm^{-1}** results from **O-H stretching** vibrations that primarily assigned to hydroxyl groups present in gelatin and PEG[66]. This result correlates with the abundant water content observed in natural breast tissues. The absorption peak at **2928 cm^{-1}** results from **C-H stretching** vibrations because it indicates the hydrocarbon chain distribution in vegetable oil. This mimics the lipid content found in the real breast tissues. A strong intense peak appears at **1628 cm^{-1}** which represents the **Amide I** band resulting from **C=O stretching** vibrations in the

peptide bond of gelatin. The peak appeared at **1537 cm^{-1}** corresponds to the **Amide II** representing the **N-H bending** and **C-N stretching** of the amide groups within gelatin. Since gelatin works as a collagen derivative which replicates the protein components present in real breast tissue. The peak located at **1448 cm^{-1}** shows **CH_2 bending** vibrations due to vegetable oil materials which mimic the fatty acid and lipid content found in human breast tissue. The peak at **1332 cm^{-1}** results from **C-H bending** from both gelatin and PEG components[67]. The peak at **1236 cm^{-1}** corresponds to the **Amide III** resulting from **C-N stretching** confirming the protein structure contributed by gelatin. The signals at **1160 cm^{-1}** and **1034 cm^{-1}** belong to **C-O-C asymmetric stretching** and **C-O stretching** vibrations which originate from agar and PEG components that mimics the polysaccharide and carbohydrate content of real breast tissue[53][64].

Table 1 FTIR of Tumor Layer

Wavelength (cm^{-1})	**Material Used**	**Corresponding Functional Group**	**Common Biological Components**
1628 1537 1236	Gelatin	C=O stretching N-H bending C-N stretching	Protein (Amide I) Protein (Amide II) Protein (Amide III)
1160 1034	Agar	C-O-C stretching C-O stretching	Polysaccharides Carbohydrates
3272 1160	Polyethylene Glycol (PEG)	O-H stretching C-O-C stretching	water retention
2928 1448	Vegetable Oil	C-H stretching CH_2 bending	Lipid and fatty acid chains (adipose tissue)

4.1.2 FTIR Analysis of Silver oxide nanoparticles:

The FTIR spectrum analyzes the synthesized silver oxide nanoparticles to detect all the functional groups. The investigation of FTIR analysis operated within the wave number range of 500 cm^{-1} – 4000 cm^{-1}.

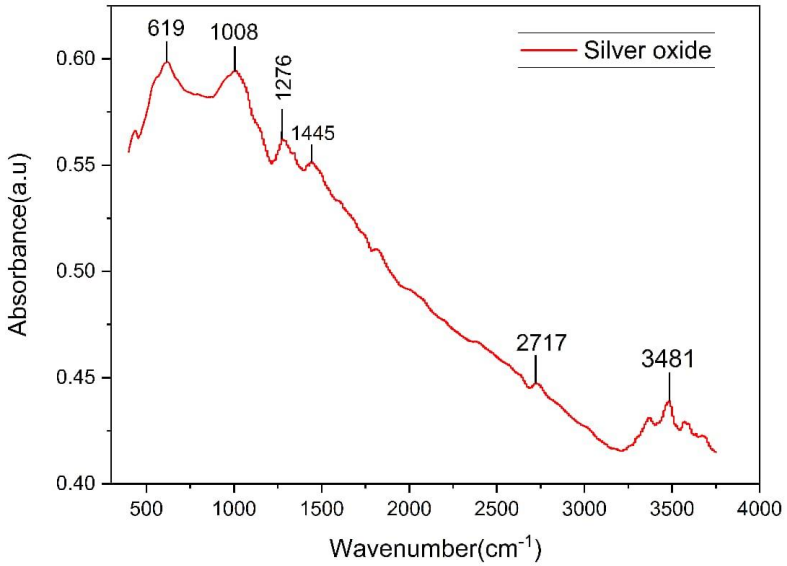

Figure 4.2 FTIR of Silver Oxide NPs

Table 2 FTIR of Silver Oxide NPs

Wavenumber (cm^{-1})	Functional Group	Vibrational Mode	Common Chemical Component
600–1000	Ag–O C–O	Stretching	Silver(I) oxide
1000–1300	C–O	Stretching	Ethanol
1300–1500	CH_2	Bending	Hexane
2700–2800	C–H	Stretching	Formaldehyde
3200–3550	O–H	Stretching	Water

FTIR analysis was conducted to investigate the functional groups, chemical bonding characteristics, and structural signatures associated with the synthesized silver oxide nanoparticles and their interaction within the phantom matrix. The smoothed FTIR spectrum of the Ag_2O sample displayed distinct vibrational features

linked to metal–oxygen bonding and organic residues originating from the synthesis and phantom formulation materials. A characteristic absorption band appearing near **520–650 cm^{-1}** corresponds to the Ag–O stretching vibration, confirming the successful formation of silver oxide nanoparticles. Additional peaks observed in the **1540–1690 cm^{-1}** range are attributed to C=O stretching and N–H bending vibrations, which represent residual organic compounds derived from gelatin, PEG, and other polymeric additives used in the phantom preparation[68].

A broad absorption feature above **3600 cm^{-1}** corresponds to O–H stretching, indicating moisture retention and hydrogen bonding interactions within the hydrogel-based phantom structure. Furthermore, peaks detected near **1266 cm^{-1}** relate to C–O stretching modes associated with polymer chains and stabilizing agents within the nanoparticle matrix.

Overall, the FTIR analysis confirms the formation of Ag–O bonds, verifying the successful synthesis of silver oxide nanoparticles. The presence of organic functional groups reflects strong nanoparticle–matrix interactions, suggesting stable dispersion within the phantom. These findings indicate that the synthesized Ag_2O nanoparticles are chemically compatible with the phantom composition and structurally suitable for imaging applications, particularly CT-based contrast enhancement due to the metal–oxygen bond formation and stable nanoparticle incorporation[68].

4.1.3 FTIR Analysis of Iron oxide nanoparticles:

The FTIR spectrum analyzes the synthesized silver oxide nanoparticles to detect all the functional groups. The investigation of FTIR analysis operated within the wave number range of 500 cm^{-1} – 4000 cm^{-1}.

FTIR spectrum of Iron oxide's exhibits distinctive absorption bands that verify the creation of Fe_3O_4 nanoparticles. Fe–O stretching vibrations, the fingerprint band of iron oxide, are shown by the prominent peak at about 690 cm^{-1}, which verifies the effective production of nanoparticles. The band at around 1360 cm^{-1} is thought to be caused by C–O stretching, which comes from stabilizing chemicals or leftover organic species from the synthesis process. C=O stretching vibrations are responsible for the absorption peak at around 1650 cm^{-1}, which suggests the existence of carbonyl groups from citric acid or other organic precursors. O=C=O, a weak band about ~2350 cm^{-1}, is frequently linked to atmospheric CO_2 adsorption. O–H stretching vibrations are responsible for the broad absorption bands seen at around 3280 cm^{-1} and 3720 cm^{-1}, which verify the existence of surface hydroxyl groups and adsorbed moisture[69].

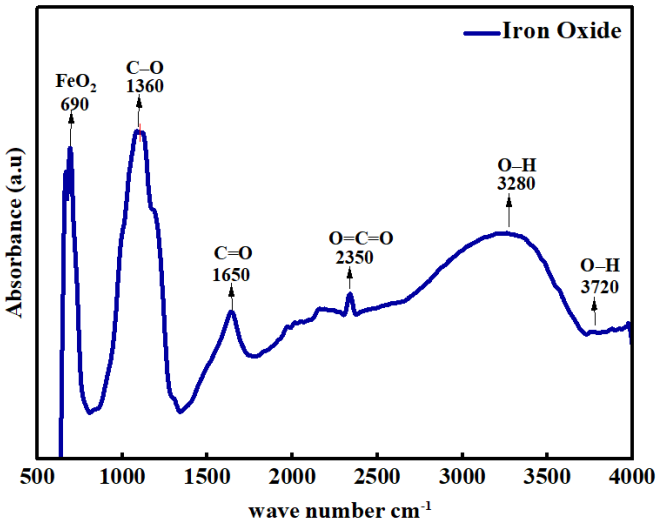

Figure 4.3 FTIR of Iron Oxide NPs

The production of iron oxide nanoparticles with surface hydroxylation and trace organic residues, which improve hydrophilicity and compatibility with hydrogel-based tumor phantoms, is often confirmed by the FTIR data.

Table 3 FTIR of Iron Oxide NPs

Wavenumber (cm^{-1})	Functional Group	Vibrational Mode	Chemical Component
3700–3600	O–H	Stretching	hydroxyl groups
3300–3200	O–H	Bending	OH groups
1700–1760	C=O	Stretching	Carbonyl
1300–1350	C–N	Stretching	Organic stabilizers
1050–1150	C–O	Stretching	Alcohol
800–600	Fe–O	Stretching	Iron oxide

4.2 XRD Analysis of Silver oxide nanoparticles:

The X-ray diffraction pattern of the synthesized silver oxide (Ag_2O) nanoparticles shows distinct diffraction peaks that confirm the formation of a crystalline Ag_2O phase. The smooth intensity profile with sharp peak shapes indicates well-developed crystallinity and uniform particle structure. Major reflections observed in the pattern correspond to the face-centered cubic (FCC) lattice of Ag_2O, typically indexed to the (111), (200), (220), and (311) crystallographic planes. These diffraction signatures match the standard reference data for Ag_2O reported in the JCPDS database, verifying the phase purity of the synthesized sample[70].

Table 4 XRD of Silver Oxide NPs

2θ	(hkl)
38.1°	(111)
44.3°	(200)
64.4°	(220)
77.5°	(311)

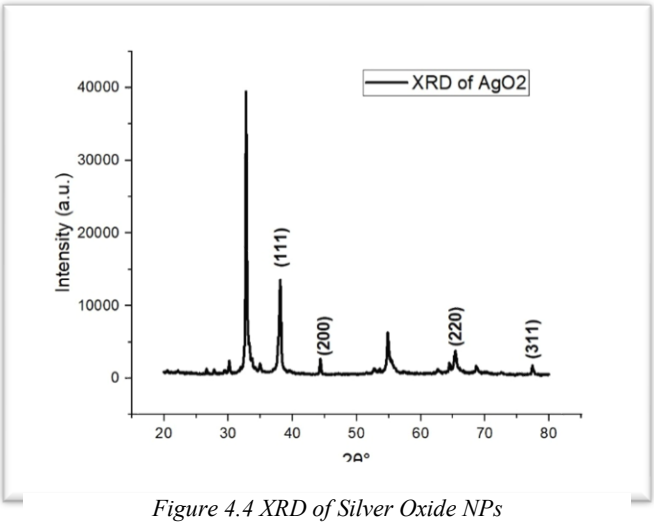

Figure 4.4 XRD of Silver Oxide NPs

The absence of additional or unexpected diffraction peaks suggests that no secondary phases, such as metallic Ag or Ag_2O, were formed during synthesis. This confirms successful oxidation of silver precursor ions and controlled growth conditions throughout the precipitation process. The high-intensity peak associated with the (111) plane reflects the preferred crystal orientation, which is commonly observed in silver-based nanoparticles and indicates stable, uniform grain development.

Overall, the XRD analysis validates the formation of phase-pure Ag_2O nanoparticles with a crystalline FCC structure. These results confirm successful

synthesis and structural integrity, supporting the suitability of the prepared nanoparticles for biomedical and CT imaging applications due to their strong radiographic contrast behavior and stable nanostructure formation[71].

4.2.1 XRD Analysis of Iron oxide nanoparticles:

The well-defined diffraction peaks in the iron oxide XR pattern verify that the produced nanoparticles are crystalline. The significant reflections seen at 2θ values that correspond to the (220), (311), (400), and (440) planes are indicative of cubic spinel Fe_3O_4 (magnetite). The (311) plane is the most intense of all, suggesting that crystal formation prefers this orientation. A low-intensity peak close to (012) indicates small crystallographic contributions, which might be caused by surface effects or a little amount of nanoscale structural instability. High phase purity of the iron oxide nanoparticles is shown by the lack of additional impurity peaks. Overall, the XRD results show the single-phase, crystalline Fe3O4 nanoparticles were successfully formed, making them appropriate for phantom-based diagnostic imaging contrast[70].

Table 5 XRD of Iron Oxide

2θ	(hkl)
24.2°	(012)
33.1°	(220)
35.5°	(311)
43.2°	(400)
62.7°	(440)

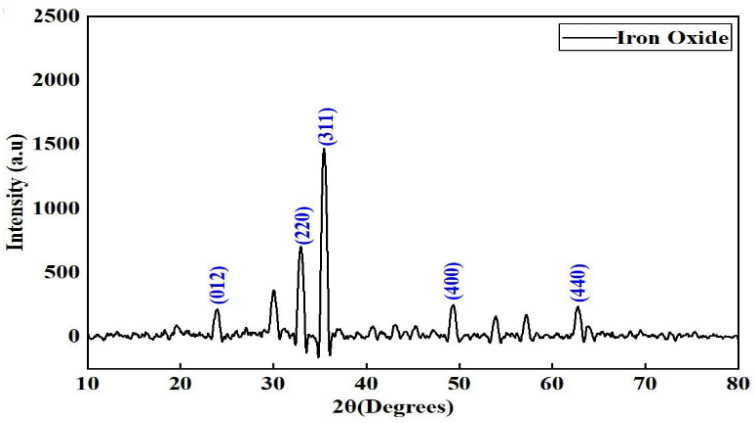

Figure 4.5 XRD Of Iron Oxide NPs

4.3 SEM of Silver oxide nanoparticles

Through Scanning Electron Microscopy (SEM), the surface morphology and shape of the synthesized silver oxide nanoparticles were characterized.

Based on the result as presented in Figure 4.5 the SEM image reveals that the nanoparticles are mainly spherical to semispherical with rough surface. Some forms of agglomeration can be observed, which is expected since silver oxide nanoparticle has a strong magnetic dipole-dipole interaction, as well as high surface energy. Even then,

the nanoparticles are irregular in shape and having porous texture refers to a large surface area which is beneficial for X-ray attenuation and CT scan. The scale of the particle size can be visually estimated to be between the nanometers, which is accompanied by the data collected with the help of the Dynamic Light Scattering (DLS).

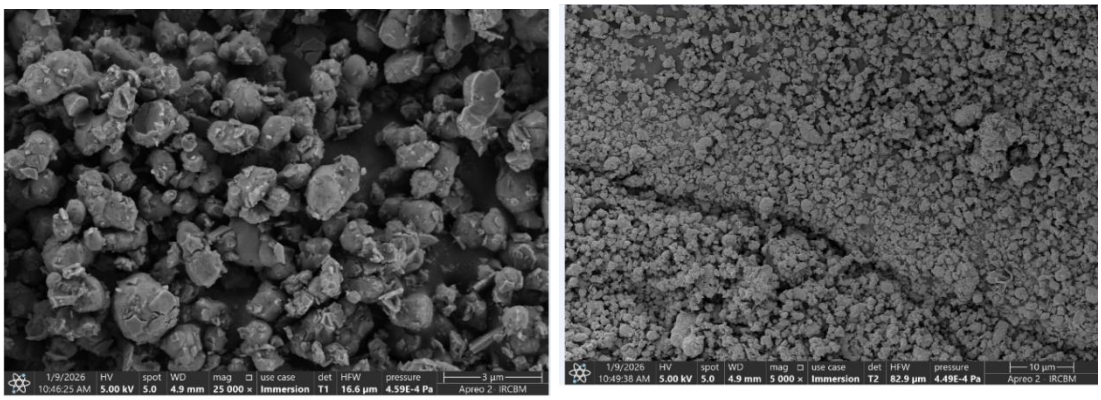

Figure 4.6 SEM of Silver Oxide NPs

4.3.1 SEM of Iron oxide nanoparticles

Through Scanning Electron Microscopy (SEM), the surface morphology and shape of the synthesized iron oxide nanoparticles were characterized. Based on the result as presented in Figure 4.5 the SEM image reveals that the nanoparticles are mainly spherical to polyhedral with uniform size distribution. Some forms of agglomeration can be observed, which is expected since iron oxide nanoparticle has a strong magnetic dipole-dipole interaction, as well as high surface energy. Even then, the nanoparticles are uniform in shape and have large surface area. The scale of the particle size can be visually estimated to be between the nanometers, which is accompanied by the data collected with the help of the Dynamic Light Scattering(DLS).

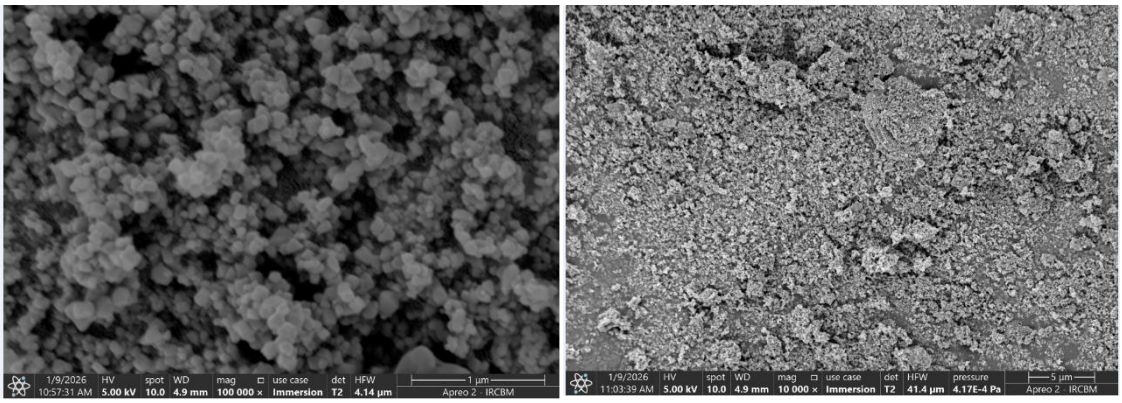

Figure 4.7 SEM of Iron Oxide

4.4 CT scan:

The CT scan analysis was conducted to evaluate the X-ray attenuation characteristics of different tissue-mimicking layers within the prepared breast phantom. The tumor layer had the greatest average CT of **129 HU** which means that it will absorb a lot of X-ray energy. Such high CT value indicates the achievement of silver and iron oxide nanoparticles elevation into the tumor matrix, which is expected to find accurate tumor boundaries as the silver and iron oxide nanoparticles have a high atomic number[72].

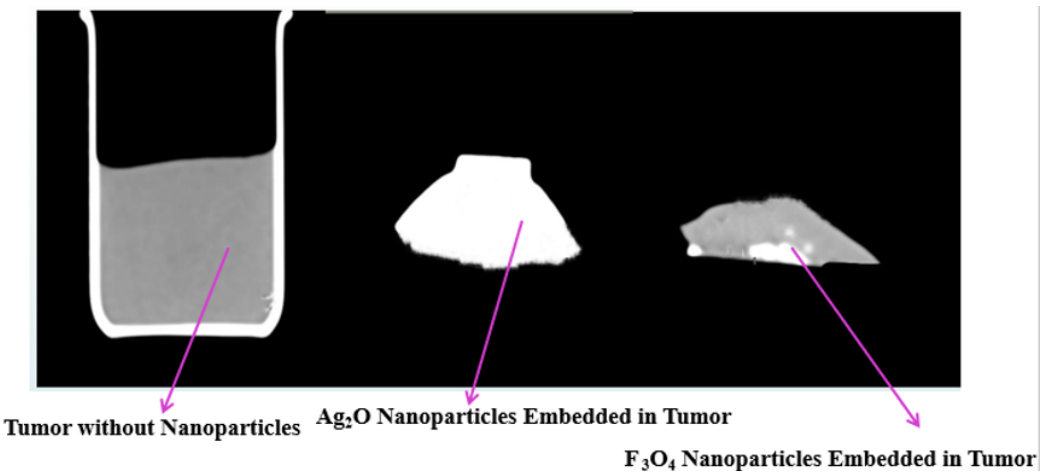

Figure 4.8 CT scan of Phantom with & without NPs

Chapter 5 Conclusion

In this study, a homogeneous breast tumor phantom embedded with dual nanoparticles of silver oxide (Ag_2O) and iron oxide (Fe_3O_4) was successfully developed to improve breast tumor visualization and diagnostic accuracy. The phantom was fabricated using a gelatin-based tissue-mimicking matrix designed to replicate the physical and radiological response of malignant breast tissue. Ag_2O and Fe_3O_4 nanoparticles were incorporated into the tumor region using an optimized premixing approach, ensuring uniform dispersion throughout the phantom and producing a stable nanoparticle-enhanced diagnostic model.

Comprehensive material characterization confirmed the authenticity of the synthesized nanoparticles and their successful integration within the phantom matrix. XRD verified the crystalline structures of Ag_2O and Fe_3O_4 nanoparticles, while FTIR analysis confirmed the presence of metal-oxygen vibrational signatures and chemical compatibility with the phantom material. Supporting morphological and size analyses further validated nanoparticle behavior suitable for biomedical imaging applications.

CT imaging demonstrated substantial contrast improvement in Ag_2O loaded phantom regions due to the high atomic number of silvers, which significantly enhanced X-ray attenuation and elevated Hounsfield Unit values. In parallel, MRI analysis revealed strong contrast suppression and signal reduction in Fe_3O_4-enhanced tumor areas, confirming their superparamagnetic behavior and improved tumor localization. These results demonstrate that embedding both nanoparticles within a homogeneous tumor phantom enables multimodal contrast capability, providing efficient diagnostic visibility across CT and MRI platforms.

Overall, the successful fabrication of a single-layer nanoparticle-embedded breast tumor phantom demonstrates strong potential for advanced breast cancer diagnosis. The homogeneous tumor structure, combined with dual nanoparticle incorporation, offers improved radiological contrast, enhanced tumor detectability, and reliable clinical imaging simulation. This phantom system provides a valuable diagnostic research tool for imaging optimization, contrast agent evaluation, and future developments in nanoparticle-assisted breast cancer detection.

Chapter 6 References

[1] J. Talapko et al., “Health Effects of Ionizing Radiation on the Human Body,” Apr. 01, 2024, Multidisciplinary Digital Publishing Institute (MDPI). doi: 10.3390/medicina60040653.

[2] L. Dinapoli, G. Colloca, B. Di Capua, and V. Valentini, “Psychological Aspects to Consider in Breast Cancer Diagnosis and Treatment,” Mar. 01, 2021, Springer. doi: 10.1007/s11912-021-01049-3.

[3] F. Pesapane et al., “How Radiomics Can Improve Breast Cancer Diagnosis and Treatment,” Feb. 01, 2023, MDPI. doi: 10.3390/jcm12041372.

[4] F. Bray et al., “Global cancer statistics 2022: GLOBOCAN estimates of incidence and mortality worldwide for 36 cancers in 185 countries,” CA Cancer J. Clin., vol. 74, no. 3, pp. 229–263, May 2024, doi: 10.3322/caac.21834.

[5] M. Dessale, G. Mengistu, and H. M. Mengist, “Nanotechnology: A Promising Approach for Cancer Diagnosis, Therapeutics and Theragnosis,” 2022, Dove Medical Press Ltd. doi: 10.2147/IJN.S378074.

[6] S. J. Glick and L. C. Ikejimba, “Advances in digital and physical anthropomorphic breast phantoms for x-ray imaging,” 2018. doi: 10.1002/mp.13110.

[7] T. T. Dongsar, T. S. Dongsar, M. A. S. Abourehab, N. Gupta, and P. Kesharwani, “Emerging application of magnetic nanoparticles for breast cancer therapy,” Eur. Polym. J., vol. 187, p. 111898, Apr. 2023, doi: 10.1016/J.EURPOLYMJ.2023.111898.

[8] H. Hosseinkazemi et al., “Applications of Iron Oxide Nanoparticles against Breast Cancer,” 2022, Hindawi Limited. doi: 10.1155/2022/6493458.

[9] C. He, Y. Guo, B. Karmakar, A. El-kott, A. E. Ahmed, and A. Khames, “Decorated silver nanoparticles on biodegradable magnetic chitosan/starch composite: Investigation of its cytotoxicity, antioxidant and anti-human breast cancer properties,” J. Environ. Chem. Eng., vol. 9, no. 6, p. 106393, Dec. 2021, doi: 10.1016/J.JECE.2021.106393.

[10] D. Barkley et al., “Cancer cell states recur across tumor types and form specific interactions with the tumor microenvironment,” Nat. Genet., vol. 54, no. 8, pp. 1192–1201, Aug. 2022, doi: 10.1038/s41588-022-01141-9.

[11] P. J. Bazira, H. Ellis, and V. Mahadevan, “Anatomy and physiology of the breast,” Surgery (Oxford), vol. 40, no. 2, pp. 79–83, Feb. 2022, doi: 10.1016/J.MPSUR.2021.11.015.

[12] H. N. Mayrovitz, “Breast Cancer.”

[13] F. Mahjabeen, S. F. Habbani, and S. I. Mohammed, “Molecular Mechanisms of Lymphatic Metastasis in Breast Cancer: An Updated Review,” Jul. 01, 2025,

Multidisciplinary Digital Publishing Institute (MDPI). doi: 10.3390/cancers17132134.

[14] S. A. Khan et al., “Early Local Therapy for the Primary Site in De Novo Stage IV Breast Cancer: Results of a Randomized Clinical Trial (EA2108),” in Journal of Clinical Oncology, American Society of Clinical Oncology, Mar. 2022, pp. 978–987. doi: 10.1200/JCO.21.02006.

[15] M. I. Hall et al., “A reinterpretation of human breast anatomy includes all the layers of the anterior body wall,” Anatomical Record, vol. 307, no. 11, pp. 3564–3573, Nov. 2024, doi: 10.1002/ar.25456.

[16] M. Higgins, S. Leung, and N. Radacsi, “3D printing surgical phantoms and their role in the visualization of medical procedures,” Annals of 3D Printed Medicine, vol. 6, p. 100057, Jun. 2022, doi: 10.1016/J.STLM.2022.100057.

[17] E. Lennie, C. Tsoumpas, and S. Sourbron, “Multimodal phantoms for clinical PET/MRI,” Dec. 01, 2021, Springer Science and Business Media Deutschland GmbH. doi: 10.1186/s40658-021-00408-0.

[18] A. Sarno, C. Valero, R. M. Tucciariello, N. Dukov, P. R. Costa, and A. Tomal, “Physical and digital phantoms for 2D and 3D x-ray breast imaging: Review on the state-of-the-art and future prospects,” Radiation Physics and Chemistry, vol. 204, p. 110715, Mar. 2023, doi: 10.1016/J.RADPHYSCHEM.2022.110715.

[19] F. E. Zerrad et al., “Symmetrical and Asymmetrical Breast Phantoms With 3D-Printed Anatomical Structure for Microwave Imaging of Breast Cancer,” IEEE Access, vol. 10, pp. 96896–96908, 2022, doi: 10.1109/ACCESS.2022.3205004.

[20] K. F. Stupic et al., “A standard system phantom for magnetic resonance imaging,” Sep. 01, 2021, John Wiley and Sons Inc. doi: 10.1002/mrm.28779.

[21] E. Lennie, C. Tsoumpas, and S. Sourbron, “Multimodal phantoms for clinical PET/MRI,” Dec. 01, 2021, Springer Science and Business Media Deutschland GmbH. doi: 10.1186/s40658-021-00408-0.

[22] N. Okkalidis, “3D printing methods for radiological anthropomorphic phantoms,” Aug. 07, 2022, Institute of Physics. doi: 10.1088/1361-6560/ac80e7.

[23] d. H. M. Y. And r. Y. N.ukhrowiyah, “fabrication and characterization of breast phantombased on gelatin-glycerin-tio2for a continuous-wave diffuse optical tomography,” malaysian journal of science, vol. 38, no. 3, pp. 53–65, nov. 2019.

[24] L. B. Christie et al., “Review of imaging test phantoms,” J. Biomed. Opt., vol. 28, no. 08, 2023, doi: 10.1117/1.jbo.28.8.080903.

[25] A. Bhushan, A. Gonsalves, and J. U. Menon, “Current state of breast cancer diagnosis, treatment, and theranostics,” May 01, 2021, MDPI. doi: 10.3390/pharmaceutics13050723.

[26] J. Baranwal, B. Barse, A. Di Petrillo, G. Gatto, L. Pilia, and A. Kumar, “Nanoparticles in Cancer Diagnosis and Treatment,” Aug. 01, 2023, Multidisciplinary Digital Publishing Institute (MDPI). doi: 10.3390/ma16155354.

[27] G. Christyani, M. Carswell, S. Qin, and W. Kim, “An Overview of Advances in Rare Cancer Diagnosis and Treatment,” Jan. 01, 2024, Multidisciplinary Digital Publishing Institute (MDPI). doi: 10.3390/ijms25021201.

[28] L. Shang, X. Zhou, J. Zhang, Y. Shi, and L. Zhong, “Metal nanoparticles for photodynamic therapy: A potential treatment for breast cancer,” Nov. 01, 2021, MDPI. doi: 10.3390/molecules26216532.

[29] S. Redjili et al., “Green synthesis of silver oxide nanoparticles: Eco-friendly approach for sustainable solutions,” Ind. Crops Prod., vol. 223, p. 120168, Jan. 2025, doi: 10.1016/J.INDCROP.2024.120168.

[30] M. Asif et al., “Synthesis and Characterization of Chemically and Green-Synthesized Silver Oxide Particles for Evaluation of Antiviral and Anticancer Activity,” Pharmaceuticals, vol. 17, no. 7, Jul. 2024, doi: 10.3390/ph17070908.

[31] M. D. Salman, Y. M. Radzi, A. A. Rahman, A. A. Oglat, and M. A. Dheyab, “Advancements and applications of dosimetry techniques in modern medical radiation therapy: a comprehensive review,” J. Radioanal. Nucl. Chem., vol. 333, no. 8, pp. 3713–3737, 2024, doi: 10.1007/s10967-024-09517-3.

[32] M. A. Anugrah, S. Ilyas, and D. Tahir, “Gelatin/Poly (vinyl alcohol)/Inorganic filler composites for phantom breasts,” Mater. Chem. Phys., vol. 262, p. 124333, Apr. 2021, doi: 10.1016/J.MATCHEMPHYS.2021.124333.

[33] M. A. Anugrah, S. Ilyas, and D. Tahir, “Gelatin/Poly (vinyl alcohol)/Inorganic filler composites for phantom breasts,” Mater. Chem. Phys., vol. 262, p. 124333, Apr. 2021, doi: 10.1016/J.MATCHEMPHYS.2021.124333.

[34] M. A. Anugrah et al., “Composite gelatin/Rhizophora SPP particleboards/PVA for soft tissue phantom applications,” Radiation Physics and Chemistry, vol. 173, p. 108878, Aug. 2020, doi: 10.1016/J.RADPHYSCHEM.2020.108878.

[35] T. Slanina, D. H. Nguyen, J. Moll, and V. Krozer, “Temperature dependence studies of tissue-mimicking phantoms for ultra-wideband microwave breast tumor detection,” Biomed. Phys. Eng. Express, vol. 8, no. 5, Sep. 2022, doi: 10.1088/2057-1976/ac811b.

[36] M. Kumar Sharma, S. P. Singh, P. Badola, M. Kumar, J. P. Saini, and A. Lay Ekuakille, “Noninvasive Microwave-Multielement Sensor for Breast Phantoms Analysis and Tumor Detection,” IEEE Sens. J., vol. 23, no. 17, 2023, doi: 10.1109/JSEN.2023.3296740.

[37] K. Ponsanti, B. Tangnorawich, N. Ngernyuang, and C. Pechyen, “Synthesis of mesoporous silica nanoparticles (MSNs)/silver nanoparticles (AgNPs): promising hybrid materials for detection of breast cancer cells,” Journal of

Materials Science: Materials in Electronics, vol. 33, no. 10, 2022, doi: 10.1007/s10854-022-07891-w.

[38] A. Dhaka, S. Chand Mali, S. Sharma, and R. Trivedi, “A review on biological synthesis of silver nanoparticles and their potential applications,” Results Chem., vol. 6, p. 101108, Dec. 2023, doi: 10.1016/J.RECHEM.2023.101108.

[39] A. Meher et al., “Silver nanoparticle for biomedical applications: A review,” Hybrid Advances, vol. 6, p. 100184, Aug. 2024, doi: 10.1016/J.HYBADV.2024.100184.

[40] D. Chicea, A. Nicolae-Maranciuc, and L. M. Chicea, “Silver Nanoparticles-Chitosan Nanocomposites: A Comparative Study Regarding Different Chemical Syntheses Procedures and Their Antibacterial Effect,” Materials, vol. 17, no. 5, Mar. 2024, doi: 10.3390/ma17051113.

[41] Reshma et al., “Synthesis, Characterization, Biological Activity of PEG Capped Silver Nanoparticles and Photocatalytic Degradation of Methylene Blue Dye using LC-MS Method,” Asian Journal of Chemistry, vol. 35, no. 11, pp. 2715–2725, Nov. 2023, doi: 10.14233/ajchem.2023.27005.

[42] Reshma et al., “Synthesis, Characterization, Biological Activity of PEG Capped Silver Nanoparticles and Photocatalytic Degradation of Methylene Blue Dye using LC-MS Method,” Asian Journal of Chemistry, vol. 35, no. 11, pp. 2715–2725, Nov. 2023, doi: 10.14233/ajchem.2023.27005.

[43] H. J. Hassan and A. Y. Alam, “SYNTHESIS AND CHARACTERIZATION OF MAGNESIUM OXIDE-DOPED IRON (III) OXIDE NANOPARTICLES BY SOL-GEL METHOD,” J. Teknol., vol. 87, no. 5, pp. 907–914, Sep. 2025, doi: 10.11113/jurnalteknologi.v87.22988.

[44] R. S. Matos et al., “Defect-enhanced Visible-light Photocatalysis in α–Fe2O3 Nanoparticles Synthesized via a Maytenus rigida-assisted Sol-Gel Method,” Appl. Surf. Sci., vol. 714, p. 164420, Dec. 2025, doi: 10.1016/J.APSUSC.2025.164420.

[45] M. B. Polla et al., “Low-temperature sol–gel synthesis of magnetite superparamagnetic nanoparticles: Influence of heat treatment and citrate–nitrate equivalence ratio,” Ceram. Int., vol. 49, no. 5, pp. 7322–7332, Mar. 2023, doi: 10.1016/J.CERAMINT.2022.10.182.

[46] G. Sadullahoglu, “Optimization of Properties of Iron Oxide Nanoparticles Synthized by Sol-Gel Method,” Technology, Engineering & Mathematics (EPSTEM), vol. 28, 2024, [Online]. Available: www.isres.org

[47] J. G. Ovejero, M. A. Garcia, and P. Herrasti, “Self-assembly of au-fe3o4 hybrid nanoparticles using a sol–gel pechini method,” Molecules, vol. 26, no. 22, Nov. 2021, doi: 10.3390/molecules26226943.

[48] M. B. Polla et al., “Low-temperature sol–gel synthesis of magnetite superparamagnetic nanoparticles: Influence of heat treatment and citrate–nitrate

equivalence ratio," Ceram. Int., vol. 49, no. 5, 2023, doi: 10.1016/j.ceramint.2022.10.182.

[49] K. Bliznakova et al., "Assessment of physical phantoms produced in the PHENOMENO project utilizing three fused filament fabrication approaches," Physica Medica, vol. 136, Aug. 2025, doi: 10.1016/j.ejmp.2025.105061.

[50] J. Islam and K. E. Mis Solval, "Recent Advancements in Marine Collagen: Exploring New Sources, Processing Approaches, and Nutritional Applications," May 01, 2025, Multidisciplinary Digital Publishing Institute (MDPI). doi: 10.3390/md23050190.

[51] H. López-Calderón et al., "Fabrication and Dielectric Characterization of Stable Oil in Gelatin Breast Tissue Phantoms for Microwave Biomedical Imaging," Micromachines (Basel)., vol. 16, no. 10, Oct. 2025, doi: 10.3390/mi16101189.

[52] A. Jawli, G. Nabi, and Z. Huang, "A Polyvinyl Alcohol (PVA)-Based Phantom for Prostate Cancer Detection Using Multiparametric Ultrasound: A Validation Study," Bioengineering, vol. 11, no. 11, Nov. 2024, doi: 10.3390/bioengineering11111052.

[53] A. Jawli, G. Nabi, and Z. Huang, "A Polyvinyl Alcohol (PVA)-Based Phantom for Prostate Cancer Detection Using Multiparametric Ultrasound: A Validation Study," Bioengineering, vol. 11, no. 11, Nov. 2024, doi: 10.3390/bioengineering11111052.

[54] A. De Jesus Aragão, D. Carvalho, B. Sanches, and W. A. M. Van Noije, "A Review on Microwave Imaging Systems for Breast Cancer Detection," 2024, Institute of Electrical and Electronics Engineers Inc. doi: 10.1109/ACCESS.2024.3516762.

[55] B. Bogaert, L. Mijjer, and M. Otter, "Agar/NaCl Tissue Phantom Mimicking Electrical Properties of Human Body in Low Frequency Spectrum A Brain-Computer Interface Inside Your Earphones Electrical Engineering Programme."

[56] A. Antoniou et al., "Utilizing an Agar/Silica Phantom for Magnetic Resonance Imaging-guided Focused Ultrasound Evaluation: Lesion Formation, Magnetic Resonance Imaging Manifestation, and Comparison with Porcine Tissue," J. Med. Ultrasound, Aug. 2025, doi: 10.4103/jmu.jmu-d-25-00008.

[57] M. Caballo et al., "Patient-derived heterogeneous breast phantoms for advanced dosimetry in mammography and tomosynthesis," Med. Phys., vol. 49, no. 8, pp. 5423–5438, Aug. 2022, doi: 10.1002/mp.15785.

[58] A. Harun et al., "3D Tumor-Mimicking Phantom Models for Assessing NIR I/II Nanoparticles in Fluorescence-Guided Surgical Interventions," ACS Nano, vol. 19, no. 21, pp. 19757–19776, Jun. 2025, doi: 10.1021/acsnano.5c01919.

[59] G. Jozanikohan and M. N. Abarghooei, "The Fourier transform infrared spectroscopy (FTIR) analysis for the clay mineralogy studies in a clastic reservoir," J. Pet. Explor. Prod. Technol., vol. 12, no. 8, pp. 2093–2106, Aug. 2022, doi: 10.1007/s13202-021-01449-y.

[60] S. Nasiri et al., “Modified Scherrer equation to calculate crystal size by XRD with high accuracy, examples Fe2O3, TiO2 and V2O5,” Nano Trends, vol. 3, p. 100015, Sep. 2023, doi: 10.1016/J.NWNANO.2023.100015.

[61] J. Gallet et al., “Experimental measurement of dislocation density in metallic materials: A quantitative comparison between measurements techniques (XRD, R-ECCI, HR-EBSD, TEM),” Mater. Charact., vol. 199, p. 112842, May 2023, doi: 10.1016/J.MATCHAR.2023.112842.

[62] A. Ali, N. Zhang, and R. M. Santos, “Mineral Characterization Using Scanning Electron Microscopy (SEM): A Review of the Fundamentals, Advancements, and Research Directions,” Dec. 01, 2023, Multidisciplinary Digital Publishing Institute (MDPI). doi: 10.3390/app132312600.

[63] D. Koga, S. Kusumi, H. Yagi, and K. Kato, “Three-dimensional analysis of the intracellular architecture by scanning electron microscopy,” Jun. 01, 2024, Oxford University Press. doi: 10.1093/jmicro/dfad050.

[64] F. Sadeghi, P. Sheikhzadeh, S. Farzanehfar, P. Ghafarian, Y. Moafpurian, and M. Ay, “The effects of various penalty parameter values in Q.Clear algorithm for rectal cancer detection on 18F-FDG images using a BGO-based PET/CT scanner: a phantom and clinical study,” EJNMMI Phys., vol. 10, no. 1, Dec. 2023, doi: 10.1186/s40658-023-00587-y.

[65] Y. Li et al., “A phantom study comparing low-dose CT physical image quality from five different CT scanners,” Quant. Imaging Med. Surg., vol. 12, no. 1, pp. 766–780, Jan. 2022, doi: 10.21037/qims-21-245.

[66] P. Wang et al., “A disulfiram/copper gluconate co-loaded bi-layered long-term drug delivery system for intraperitoneal treatment of peritoneal carcinomatosis,” Colloids Surf. B Biointerfaces, vol. 231, p. 113558, Nov. 2023, doi: 10.1016/J.COLSURFB.2023.113558.

[67] C. Chen, F. Chen, B. Yang, K. Zhang, X. Lv, and C. Chen, “A novel diagnostic method: FT-IR, Raman and derivative spectroscopy fusion technology for the rapid diagnosis of renal cell carcinoma serum,” Spectrochim. Acta A Mol. Biomol. Spectrosc., vol. 269, p. 120684, Mar. 2022, doi: 10.1016/J.SAA.2021.120684.

[68] O. Yildirim, D. Tunay, B. Ozkaya, and A. Demir, “Effect of Green synthesized silver oxide nanoparticle on biological hydrogen production,” Int. J. Hydrogen Energy, vol. 47, no. 45, pp. 19517–19525, May 2022, doi: 10.1016/J.IJHYDENE.2021.11.176.

[69] J. E. Ogbezode, U. S. Ezealigo, A. Bello, V. C. Anye, and A. P. Onwualu, “A narrative review of the synthesis, characterization, and applications of iron oxide nanoparticles,” Dec. 01, 2023, Springer. doi: 10.1186/s11671-023-03898-2.

[70] U. Kalsoom et al., “Biocatalytic degradation of reactive blue 221 and direct blue 297 dyes by horseradish peroxidase immobilized on iron oxide nanoparticles

with improved kinetic and thermodynamic characteristics," Chemosphere, vol. 312, p. 137095, Jan. 2023, doi: 10.1016/J.CHEMOSPHERE.2022.137095.

[71] V. I. Mohamad and A. I. Alwared, "Environmentally friendly synthesis of silver oxide nanoparticles using leaf extract from trumpet vine," Journal of Ecological Engineering, vol. 26, no. 3, pp. 135–146, 2025, doi: 10.12911/22998993/199588.

[72] I. Mutreja, N. Maalej, A. Kaushik, D. Kumar, and A. Raja, "High atomic number nanoparticles to enhance spectral CT imaging aspects," Aug. 17, 2023, Royal Society of Chemistry. doi: 10.1039/d3ma00231d.